

www.acsami.org Research Article

# Nature-Inspired Design of Nano-Architecture-Aligned Ni₅P₄-Ni₂P/NiS Arrays for Enhanced Electrocatalytic Activity of Hydrogen Evolution Reaction (HER)

Navid Attarzadeh, Debabrata Das, Srija N. Chintalapalle, Susheng Tan, V. Shutthanandan, and C. V. Ramana\*



Cite This: ACS Appl. Mater. Interfaces 2023, 15, 22036-22050



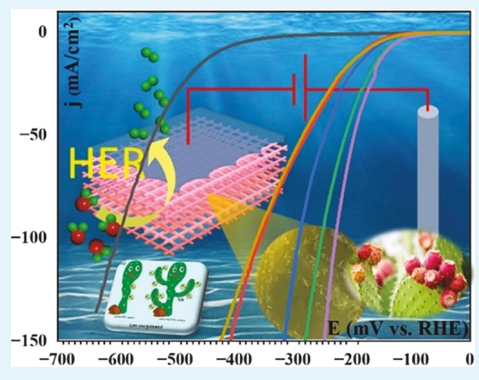
**ACCESS** I

III Metrics & More

Article Recommendations

Supporting Information

**ABSTRACT:** The projection of developing sustainable and cost-efficient electrocatalysts for hydrogen production is booming. However, the full potential of electrocatalysts fabricated from earth-abundant metals has yet to be exploited to replace Pt-group metals due to inadequate efficiency and insufficient design strategies to meet the ever-increasing demands for renewable energies. To improve the electrocatalytic performance, the primary challenge is to optimize the structure and electronic properties by enhancing the intrinsic catalytic activity and expanding the active catalytic surface area. Herein, we report synthesizing a 3D nanoarchitecture of aligned  $Ni_5P_4$ - $Ni_2P/NiS$  (plate/nanosheets) using a phosphosulfidation process. The durability and unique design of prickly pear cactus in desert environments by adsorbing moisture through its extensive surface and ability to bear fruits at the edges of leaves inspire this study to adopt a similar 3D architecture and utilize it to design an efficient heterostructure catalyst for HER activity. The catalyst



comprises two compartments of the vertically aligned  $Ni_5P_4$ - $Ni_2P$  plates and the NiS nanosheets, resembling the role of leaves and fruits in the prickly pear cactus. The  $Ni_5P_4$ - $Ni_2P$  plates deliver charges to the interface areas, and the NiS nanosheets significantly influence  $H_{ad}$  and transfer electrons for the HER activity. Indeed, the synergistic presence of heterointerfaces and the epitaxial NiS nanosheets can substantially improve the catalytic activity compared to nickel phosphide catalysts. Notably, the onset overpotential of the best-modified ternary catalysts exhibits (35 mV) half the potential required for nickel phosphide catalysts. This promising catalyst demonstrates 70 and 115 mV overpotentials to attain current densities of 10 and 100 mA cm<sup>-2</sup>, respectively. The obtained Tafel slope is 50 mV dec<sup>-1</sup>, and the measured double-layer capacitance from cyclic voltammetry (CV) for the best ternary electrocatalyst is 13.12 mF cm<sup>-2</sup>, 3 times more than the nickel phosphide electrocatalyst. Further, electrochemical impedance spectroscopy (EIS) at the cathodic potentials reveals that the lowest charge transfer resistance is linked to the best ternary electrocatalyst, ranging from 430 to 1.75  $\Omega$  cm<sup>-2</sup>. This improvement can be attributed to the acceleration of the electron exchangeability at the interfaces. Our findings demonstrate that the epitaxial NiS nanosheets expand the active catalytic surface area and simultaneously elevate the intrinsic catalytic activity by introducing heterointerfaces, which leads to accommodating more  $H_{ad}$  at the interfaces.

KEYWORDS: hydrogen evolution reaction (HER), nickel phosphosulfide, Ni<sub>5</sub>P<sub>4</sub>-Ni<sub>2</sub>P/NiS electrocatalysts, epitaxial growth, electrochemically active surface area

# ■ INTRODUCTION

The skyrocketing demand for renewable energy and the aggravation of global warming with its ominous impact on climate change emphasize the importance of research and development activities for clean and sustainable energy conversion systems.<sup>1</sup> The nascent hydrogen (H<sub>2</sub>) utilization economy is gaining popularity because of promising advances in employing state-of-the-art electrocatalysts for water splitting, reliable storage technologies, and efficient hydrogen consumption in fuel cells. The hydrogen evolution reaction (HER) is exceedingly constrained by a large dynamic overpotential beyond its thermodynamic potential during the cathodic half-

reaction of water splitting.<sup>2</sup> So far, efficient electrocatalysts derived from platinum (Pt) group metals (PGM) have shown slight overpotentials in a broad pH range of electrolytes, while their utilization on a large scale is limited due to the scarcity and their high cost.<sup>3</sup> Therefore, the paramount challenge is to

Received: January 17, 2023 Accepted: April 11, 2023 Published: April 26, 2023





explore novel methods for synthesizing low-cost and highly active electrocatalysts with high durability and relatively low overpotentials that can be substituted with PGM catalysts.<sup>4</sup> Transition-metal phosphides (TMPs) with metalloid compounds demonstrate widespread utilization for promoting the HER due to outstanding characteristics such as high durability, intrinsic catalytic activity, and good electrical connectivity.<sup>4-6</sup> Several strategies have been offered to develop high-performance electrocatalysts. These strategies can be categorized as enhancing the intrinsic activity of individual catalytic sites,<sup>7,8</sup> increasing the population of active catalytic sites, fabricating seamless and 3D nanoarchitecture with highly conductive electrocatalysts, 10 and developing intermediate phases with suitable specific adsorption/desorption energy. 11,12 While numerous modifications were implemented to the structure, composition, and synthesizing methods of TMPs to develop versatile catalysts, 13 finding alternatives for PGM catalysts demands substantial progress to fulfill the requirements for sustainable hydrogen production. Furthermore, in the context of advancements to be made, a detailed fundamental understanding of the materials is the key, and strategies, especially those that we see routinely and last long enough in nature, must be adopted to design and unlock the potential of electrocatalysts.

For transition-metal phosphides, the consensus is that P centers in P-terminated surfaces of metal phosphide structures are negatively charged due to the induced polarization. Therefore, it creates a greater affinity for the adsorption of H\* species by trapping positively charged protons and synergistically enhances hydrogen desorption during the electrolysis process.<sup>14</sup> Combining multiple anions is currently an emerging strategy resulting in the development of chemical complexity and structural alternation to augment overall water splitting. 15 The primary motivation for utilizing two anions with the difference in electronegativity, ionization potential, and atomic radius is to increase the population of active sites by expanding the electrochemical active surface area (ECSA) and enhancing the intrinsic catalytic activity by reducing the adsorption-free energy of intermediate reactions owing to tuning the electronic structure, thereby strengthening the electrocatalytic activity. <sup>16–18</sup> Further, the synergistic presence of P and S atoms retards the surface oxidation of sulfide/ phosphide, increasing the catalysts' durability. For instance, introducing sulfur to the surface of the prepared MoP showed significant improvements in catalytic activity and stability.

Introducing both P and S anions for developing ternary transition-metal catalysts has drawn significant attention among researchers. 9,20-23 Attention is primarily given to employing different synthesis methods, typically resulting in catalysts with various ratios of phosphide to sulfide and some degree of control over surface morphology. Luo et al. reported the preparation of three-dimensional  $NiP_{0.62}S_{0.38}$  using sequential sulfidation and phosphidation processes on a nickel foam at 300 and 500 °C for 1 and 2 h, respectively. 17 Recent studies target improving catalytic activity by optimizing the surface electronic and energy of intermediates via growing epitaxial interfaces with two different components. 22,24,25 The NiPS<sub>3</sub>/Ni<sub>2</sub>P heterojunction was constructed by in situ epitaxial growth of Ni<sub>2</sub>P on 2D NiPS<sub>3</sub> sheets using a desulfuration process under a partial H2 atmosphere, and the electrocatalyst electrodes were prepared using the drop cast method.<sup>22</sup> Liang et al. indicated modification of the electronic features of the fabricated catalysts. This study revealed that the energy barrier

for the HER at the NiPS<sub>3</sub>/Ni<sub>2</sub>P heterojunction showed a significant drop. The authors realized that the H\* affinity significantly reduced on the Ni centers. However, the current literature lacks a seamless electrocatalyst synthesized using a 3D nanoarchitecture with modified epitaxial growth and heterointerfaces structures. This approach may result in an accelerated electron transfer due to a robust electronic interaction at the interface of epitaxial sheets.

Fascinated by the aforementioned scientific challenges, herein, we report highly efficient seamless electrocatalysts synthesized by a two-step chemical vapor process on ultrathin nickel meshes manufactured by electroplating into an etchable mask. The phosphidation of the nickel mesh creates vertically aligned Ni<sub>5</sub>P<sub>4</sub>-Ni<sub>2</sub>P plates, which are used as template sites to synthesize the Ni<sub>5</sub>P<sub>4</sub>-Ni<sub>2</sub>P/NiS (plates/nanosheets) 3D structures due to in situ growth of epitaxial nanosheets and emerging abundant heterointerfaces. We hypothesize that this modification optimizes the catalytic activity for hydrogen production. The epitaxial NiS nanosheets resemble prickly pear fruits thanks to their similarity in growing at the edges of their leaves. The electrochemical studies confirm that the growth of the epitaxial NiS nanosheets on the edges and steps of Ni<sub>5</sub>P<sub>4</sub>-Ni<sub>2</sub>P plates reduces the overpotentials and the Tafel slopes, indicating a more significant number of active catalytic sites can be exposed to H\* species, and also the intrinsic catalytic activity is strengthened. The electrochemical impedance spectroscopy (EIS) results also confirm that the growth of NiS can modify the interaction with H\* species, and greater electron exchangeability prevails at interfaces. Furthermore, the prepared seamless architecture of the Ni<sub>5</sub>P<sub>4</sub>-Ni<sub>2</sub>P/NiS 3D structure not only offers a broad surface area with abundant active sites for the hydrogen evolution reaction (HER) but also facilitates hydrogen gas removal from the surface due to more significant spatial freedom compared to foam sheets.

#### EXPERIMENTAL DETAILS

A Synthesis. Preparation of porous nickel phosphide on nickel meshes: A piece of Ni mesh (1 cm × 2 cm, ~0.002 g, GOODFELLOW CAMBRIDGE Ltd.) was washed under ultrasonication in propanol and ethanol for 10 min to degrease and then rinsed with DI water and allowed to dry in an oven at 60 °C. The Ni mesh features a thickness of 0.004 mm, a wireline width of 0.011 mm, and an open area of 60% (200 wire·cm<sup>-2</sup>). Then, a quartz boat containing 0.2 g of red phosphorous powder (Sigma-Aldrich, %99.99 pure) was covered partially by Ni mesh with keeping at a 1 cm distance above the powders. After that, the boat and mesh together were placed gently inside the quartz tube of the MTI Corporation chemical vapor deposition (CVD) furnace. The tube furnace was kept under vacuum pumping, and Ar was also purged for 10 min at a flow rate of 200 SCCM to evacuate the air and replace it with Ar. The furnace was heated to 450 °C at 5 °C min<sup>-1</sup>, kept at the final temperature for 1 h, and then cooled down to room temperature at the same rate while the Ar was purged continuously during the process at the flow rate of 10 SCCM.

The growth of the epitaxial NiS nanosheets at Ni<sub>5</sub>P<sub>4</sub>-Ni<sub>2</sub>P plates: a quartz boat containing different sulfur powder shown in Table S1 with already prepared nickel phosphide structures was placed inside the furnace tube. The sulfidation process was followed according to the procedure shown in Figure S1.

B Material Characterization. We utilized various analytical techniques to characterize the structure, phase, morphology and microstructure, and chemical composition of synthesized Ni-P-S materials. Scanning electron microscopy (SEM) images were collected using Hitachi S4800 by applying 10 kV and 15  $\mu$ A. Transmission electron microscopy (TEM) images, energy-dispersive

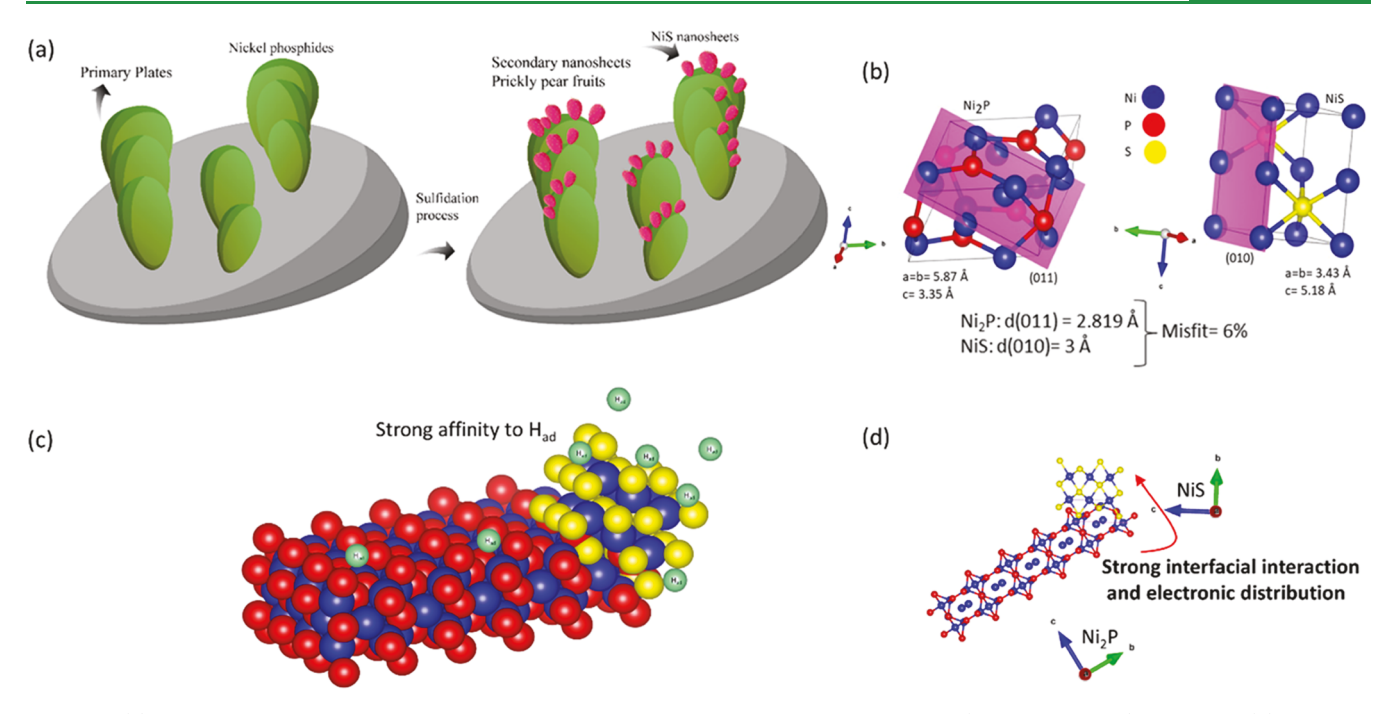


Figure 1. (a) Schematic illustration of prickly pear cactus for the generation of the Ni<sub>5</sub>P<sub>4</sub>-Ni<sub>2</sub>P/NiS (plate/nanosheets) structures, (b) Ni<sub>2</sub>P and NiS crystal structures, (c) schematic illustration for enhanced hydrogen evolution at the newly grown NiS nanosheets, (d) schematic illustration for the generation of the heterointerfaces, their synergistic interaction effects, and the crystals connections between Ni,P and NiS. Blue, red, and yellow balls represent nickel, phosphor, and sulfur, respectively.

X-ray (EDX), and selected-area electron diffraction (SAED) patterns were collected using a Thermo Scientific (formerly FEI) Titan Themis 200 with an accelerator voltage of 200 kV. X-ray diffraction (XRD) patterns were obtained using a Malvern Panalytical Empyrean Nano edition multipurpose X-ray diffractometer. To resolve peaks from the diffraction pattern, the step size and the integration time were 0.01 and 0.85 s/step, respectively. A Cu Klpha X-ray source with a wavelength of 0.154 nm was used to acquire the measurements. Rietveld refinement in X'Pert HighScore software was used to estimate the ratio of phases in the XRD pattern. X-ray photoelectron spectroscopy (XPS) scans of the best Ni-P-S electrocatalyst samples were obtained employing Kratos Axis Ultra DLD spectrometer using Al K $\alpha$  monochromatic X-ray source (1486.6 eV) and a highresolution hemispherical analyzer. The XPS survey and highresolution scans were recorded, and the data obtained were analyzed with the help of CasaXPS software employing Gaussian/Lorentzian (GL(30)) line shape, line asymmetry, and Shirley background correction.

C Electrochemical Characterization and Performance Evaluation. Hydrogen evolution reaction (HER) measurements were carried out on a Solartron analytical-ModuLab Xm workstation using a conventional three-electrode system with Ag/AgCl, a graphite rod (99.99%) as the reference electrode, and the counter electrode, respectively. The prepared electrocatalysts from ultrathin nickel mesh were working electrodes. The reference electrode was calibrated with respect to a reversible hydrogen electrode (RHE) before experiments. The electrolyte was 1.0 M H<sub>2</sub>SO<sub>4</sub> aqueous solution made from DI water. The linear sweep voltammetry (LSV) was recorded at a scan rate of 5 mV s<sup>-1</sup>. Before LSV measurement, the working electrode was kept at open-circuit potential (OCP) for 15 min to reach a pseudo-Plato voltage. The electrochemical impedance spectroscopy (EIS) was collected using the same workstation at the applied overpotentials ranging from 100 to 450 mV. The amplitude was 5 mV, while the scan started from 100 kHz to 1 Hz. IR correction was performed to account for the cell resistance based on the EIS test at the open-circuit potential (OCP). Cyclic voltammetry (CV) was performed at different scan rates ranging from 20 to 200 mV s<sup>-1</sup> and at the non-Faradaic potential region. We prepared a Pt/C (20%) electrode using the conventional method. For that, 5 mg Pt/C (20%) was sonicated

for 30 min in 1 mL solution of ethanol and Nafion (with the 9:1 ratio). We drop-cast the prepared ink on the surface of a glassy carbon electrode. Then, the HER activity of the prepared Pt/C electrode was evaluated in an identical condition that the synthesized ternary electrocatalysts were tested.

#### **RESULTS AND DISCUSSION**

A Crystal Structure, Phase, Chemical Composition, and Synthesis Process Optimization. The key to our successful synthesis of the Ni-P-S materials with desired morphology is the in-house designed chemical vapor deposition (CVD) chamber with a specific fabrication process schematically presented in Figure S1a. The fabrication process results from direct reactions between Ni mesh and chemical vapors of phosphorous and sulfur at two temperatures of 450 and 300 °C, respectively. The ultrathin Ni mesh is rationally selected to support a uniform transport of chemical vapors over the entire Ni mesh surface. The sufficient open area of Ni mesh allows efficient chemical vapor infiltration through the mesh holes during the process, leading to a uniform phase alteration on both sides of the mesh. As a promising approach, nanodomain boundaries with two or three phases can be purposefully designed to enhance electronic interactions and increase active sites simultaneously. To emphasize the critical approach of the current study, the schematic illustration in Figure 1a displays the 3D nanoarchitecture of synthesized NiPS electrocatalysts. The schematics resemble the prickly pears cactus demonstrating the result of the phosphosulfidation processes designed to improve the catalytic activity. The nickel phosphide phases, Ni<sub>5</sub>P<sub>4</sub>-Ni<sub>2</sub>P, form as vertically aligned plates during the phosphidation process resembling leaves, and the NiS nanosheets resembling the prickly pear fruits form primarily at the edge of leaves during the sulfidation process. The key novelty in the designed strategy is to synthesize a ternary system with a 3D nanoarchitecture that

provides abundant heterointerfaces and promising epitaxial NiS nanosheets. We hypothesize that the synthesized nanostructure can significantly improve the HER catalytic activity due to enhancing electronic interaction at the nanodomain scale and boundaries of different phases.

After completing the sulfidation process, we understand that a heteroepitaxial growth prevails between Ni<sub>2</sub>P and NiS phases, where the involving planes in both crystal structures are shown in Figure 1b. Indeed, heteroepitaxy is a specific case of heterogeneous nucleation in which a peculiar crystallographic relationship prevails between substrate orientation and the growing crystals. Generally, a geometric match of the dimensions between the substrate and new crystals is considered the main criterion of epitaxial growth.<sup>26</sup> In addition, the origin of the epitaxial growth can also be the structural features of the substrate crystal facets, where emerging kinks, steps, and dislocations may facilitate the epitaxial growth of a new crystalline phase.<sup>27</sup> The NiS crystallizes in the hexagonal  $P_{63}/mmc$  space group.<sup>28</sup> The involved phases of Ni<sub>5</sub>P<sub>4</sub> and Ni<sub>2</sub>P crystallize in the hexagonal  $P_{63}mc$  and  $\overline{P}_{62}m$  space groups, respectively. Beyond strengthening the electronic interaction, another aspect is the synergistic generation of heterointerfaces at the boundary of the Ni<sub>2</sub>P and NiS phases, increasing exposure at the active catalytic sites, as illustrated schematically in Figure 1c. The 2D crystal structure of Ni<sub>2</sub>P and NiS is shown in Figure 1d, where the generation of epitaxy with strong interfacial interaction led to an accelerated electron exchangeability.

X-ray diffraction (XRD) examines the composition and crystal structure of phases formed during phospho-sulfidation. Figure 2a-c shows the XRD patterns of pristine Ni mesh,

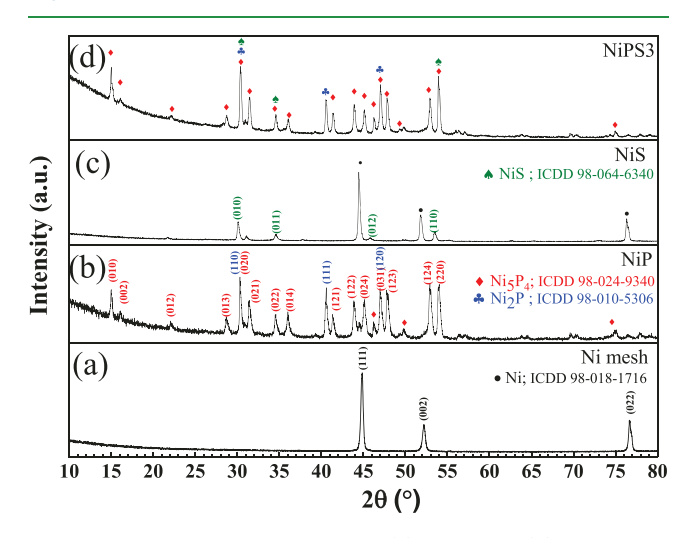


Figure 2. Powder XRD patterns for (a) Ni mesh, (b) Ni<sub>5</sub>P<sub>4</sub>-Ni<sub>2</sub>P phases, (c) NiS, and (d) heterostructure of Ni<sub>5</sub>P<sub>4</sub>-Ni<sub>2</sub>P/NiS (plates/ nanosheets).

nickel phosphide (NiP), and nickel sulfide (NiS) phases forming during the phosphidation and sulfidation processes. The XRD pattern for the ternary nickel phosphosulfide (NiPS3) is also shown in Figure 2d. After the phosphidation at 450 °C for 1 h, the XRD result in Figure 2b confirms the successful formation of two hexagonal nickel phosphide phases of Ni<sub>5</sub>P<sub>4</sub> and Ni<sub>2</sub>P, confirming previous reports by Wang et al.29 Characteristic peaks and crystallographic planes corresponding to these nickel phosphides are illustrated. The development of characteristic diffraction peaks: crystalline

planes at 15.1°: (010), 16.12°: (002), 22.12°: (012), 28.7°: (013),  $30.3^{\circ}$ : (020),  $31.4^{\circ}$ : (021),  $34.5^{\circ}$ : (022),  $36.08^{\circ}$ : (014), 41.36°: (121), 43.85°: (122), 45.16°: (024), 47°: (031), 47.8°: (123), 52.91°: (124), and 54°: (220) indicates the formation of Ni<sub>5</sub>P<sub>4</sub> (ICDD 98-024-9340) phase. Further, the development of different characteristic diffraction peaks: crystalline planes at 30.3°: (110), 40.58°: (111), and 47°: (120) represents the formation of the Ni<sub>2</sub>P (ICDD 98-064-6108) phase. These results are consistent with the nickel phosphide phases obtained from the phosphidation process of nickel foams.<sup>29,30</sup> The XRD pattern for the sulfurized mesh represents the formation of the hexagonal nickel sulfide phase of NiS, with some unreacted nickel remaining after the process (Figure 2c). The characteristic diffraction peaks: crystalline phases at  $30.11^{\circ}$ : (010),  $34.48^{\circ}$ : (011),  $44.43^{\circ}$ : (011),  $53.57^{\circ}$ : (110) are indicative of the NiS (ICDD 98-064-6340) phase. After performing the joint phosphidation and sulfidation processes consecutively, as shown in Figure S1. The XRD pattern in Figure 2d related to NiPS3 electrocatalyst reveals the formation of Ni<sub>5</sub>P<sub>4</sub> and Ni<sub>2</sub>P phases with strong diffraction peaks, while weak diffraction peaks can also be attributed to the NiS phase. Therefore, peaks corresponding to Ni<sub>5</sub>P<sub>4</sub>, Ni<sub>2</sub>P, and NiS phases are assigned in the powder XRD pattern. Raising the heating temperature at the first step can change the formed nickel phosphides' crystal structure, surface morphology, and mechanical stability. We realize that the vertical Ni<sub>5</sub>P<sub>4</sub>-Ni<sub>2</sub>P plates, used as templates for growing the NiS nanosheets, disappear after heating above 500 °C. The surface morphology alteration was also reported by Wang et al. in their study of various phases formed on the nickel foam during the phosphidation process.<sup>29</sup> They found that the formation of different nickel phases via raising the heating temperature above 500 °C decreased HER electrocatalytic activities, while the surface morphology changed and the brittleness of the foams increased. Likewise, we find out that the mechanical stability also drops significantly, where the durability of the catalysts formed at 450 °C is significant during electrochemical experiments rather than those formed at 500 °C. A quantitative analysis of the present phases is performed using the Rietveld fitting method. As shown in Figure S4, pie charts show the weight ratios of Ni<sub>5</sub>P<sub>4</sub>/Ni<sub>2</sub>P/NiS for the NiP and NiPS3 catalysts, respectively.

To reveal detailed information about the formation of different phases, particularly NiS nanosheets, we perform X-ray photoelectron spectroscopy (XPS) on the NiPS3 electrocatalyst. Thus, the chemical state and molecular environment corresponding to the formed phases are characterized using the casaXPS software. 31,32 The XPS survey spectrum in Figure 3a confirms the presence of Ni, P, and S. As shown in Figure 3b, the core-level spectra of Ni 2p<sub>3/2</sub> display a peak at 853.62 eV in the Ni 2p region, corresponding well to the  $\mathrm{Ni}^{\delta +}$  species in Ni<sub>5</sub>P<sub>4</sub>. The high-resolution XPS spectrum of the Ni 2p signal for the NiPS3 catalyst containing Ni<sub>5</sub>P<sub>4</sub>, Ni<sub>2</sub>P, and NiS phases indicates that nickel is primarily at the +3 valance state.<sup>33</sup> The appearance of the peaks at 857 and 875.42 eV are related to the Ni 2P satellite peaks. Further, the appearance of the peak at 862.76 eV in the Ni 2p spectrum of the heterostructure catalyst can be attributed to the formation of Ni-S species because of the epitaxial NiS nanosheets.<sup>34</sup> The core-level spectra of Ni 2p<sub>1/2</sub> also display a peak at 870.9 eV. Regarding the core-level P 2p spectrum (Figure 3c), the first two peaks at 130 and 130.8 eV can be assigned to the P  $2p_{3/2}$  and P  $2p_{1/2}$ , respectively. The peak at 134.2 eV can be ascribed to the P-O bond for forming

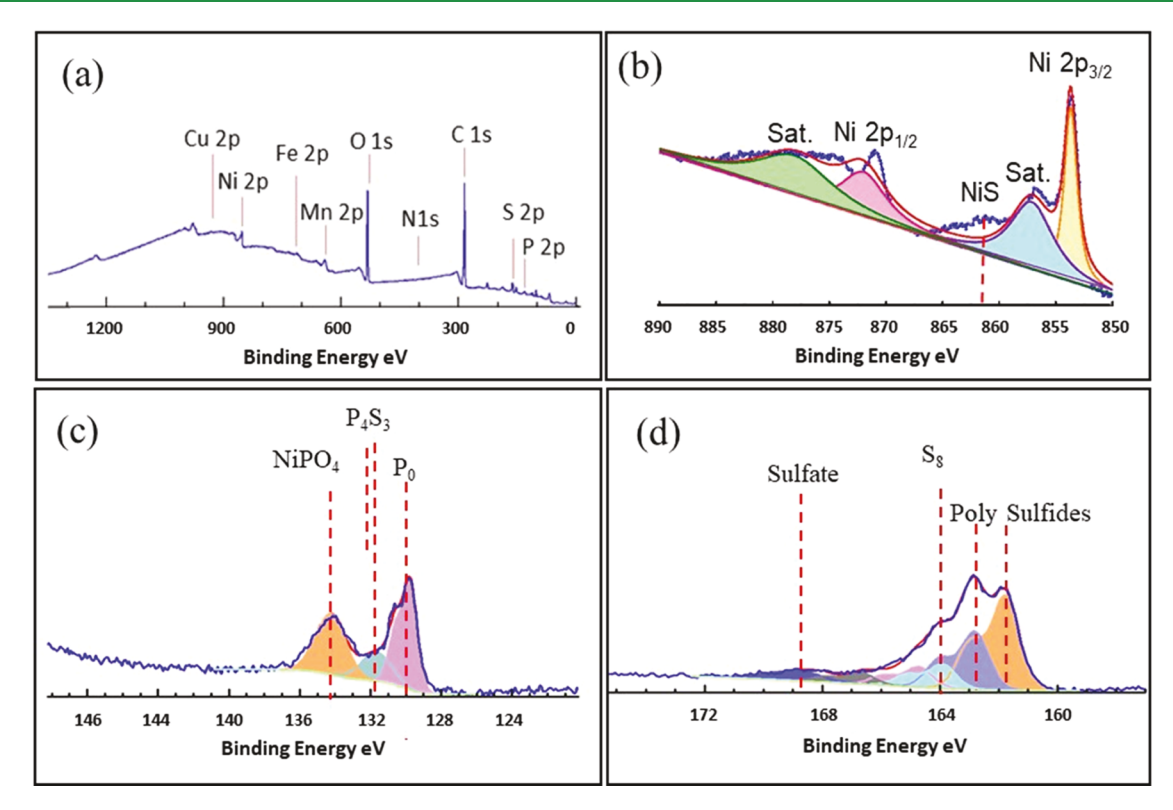


Figure 3. (a) Wide X-ray photoelectron survey for the prepared NiPS3 catalysts and high-resolution (b) Ni 2p, (c) P 2p, (d) S 2p XPS spectra of the heterostructure of  $Ni_5P_4$ - $Ni_2P/NiS$ .

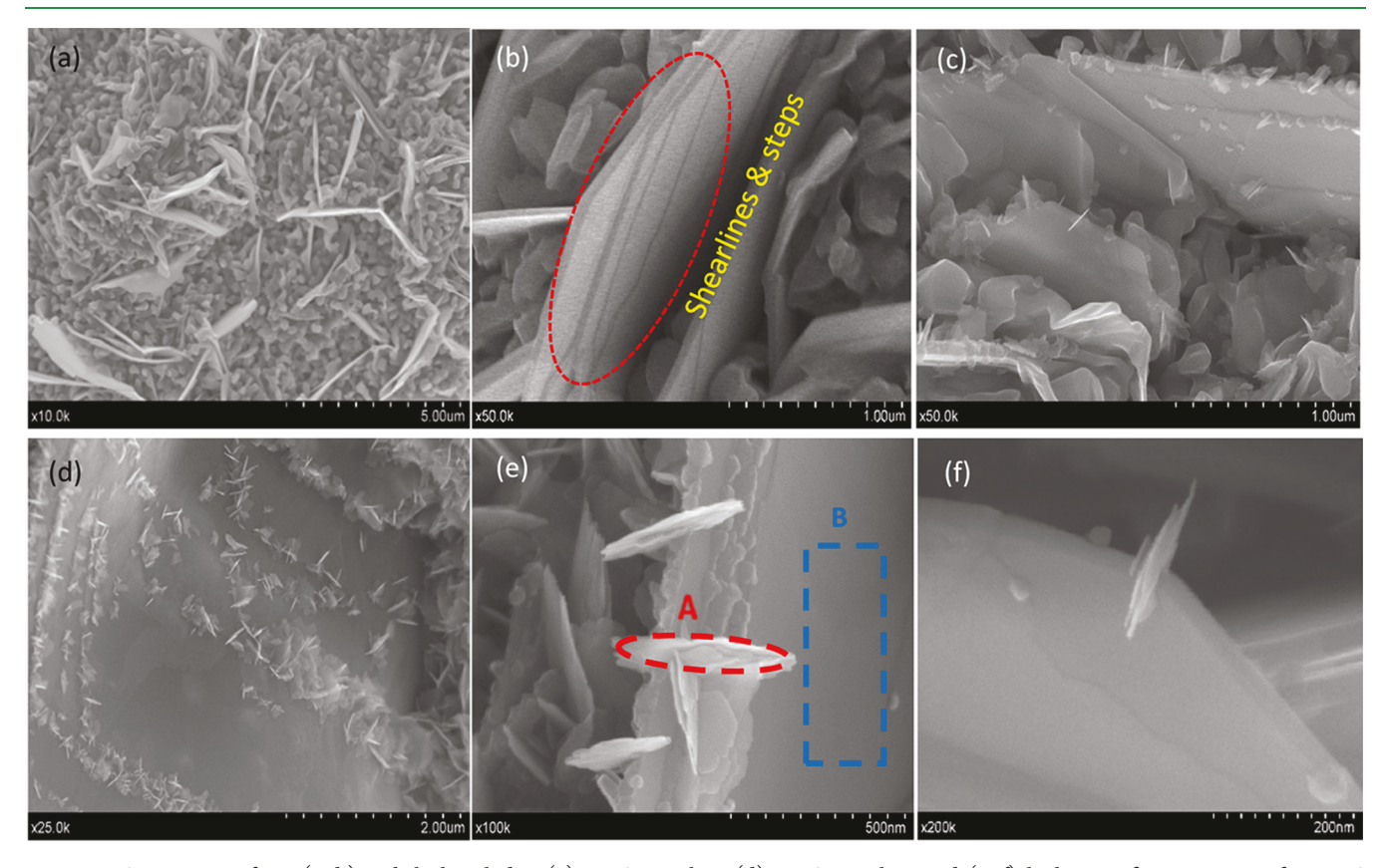


Figure 4. SEM images from (a, b) nickel phosphides, (c) NiPS1 catalyst, (d) NiPS3 catalyst, and (e, f) high-magnification images from NiS nanosheets growing at the edges.

NiPO<sub>4</sub> compounds, which is related to partial surface oxidation and agrees well with the previous study on transition-metal

phosphides.<sup>33</sup> Noticeably, we realize the peak emerging at 131.9 eV is related to the formation of  $P_4S_3$  compounds due to

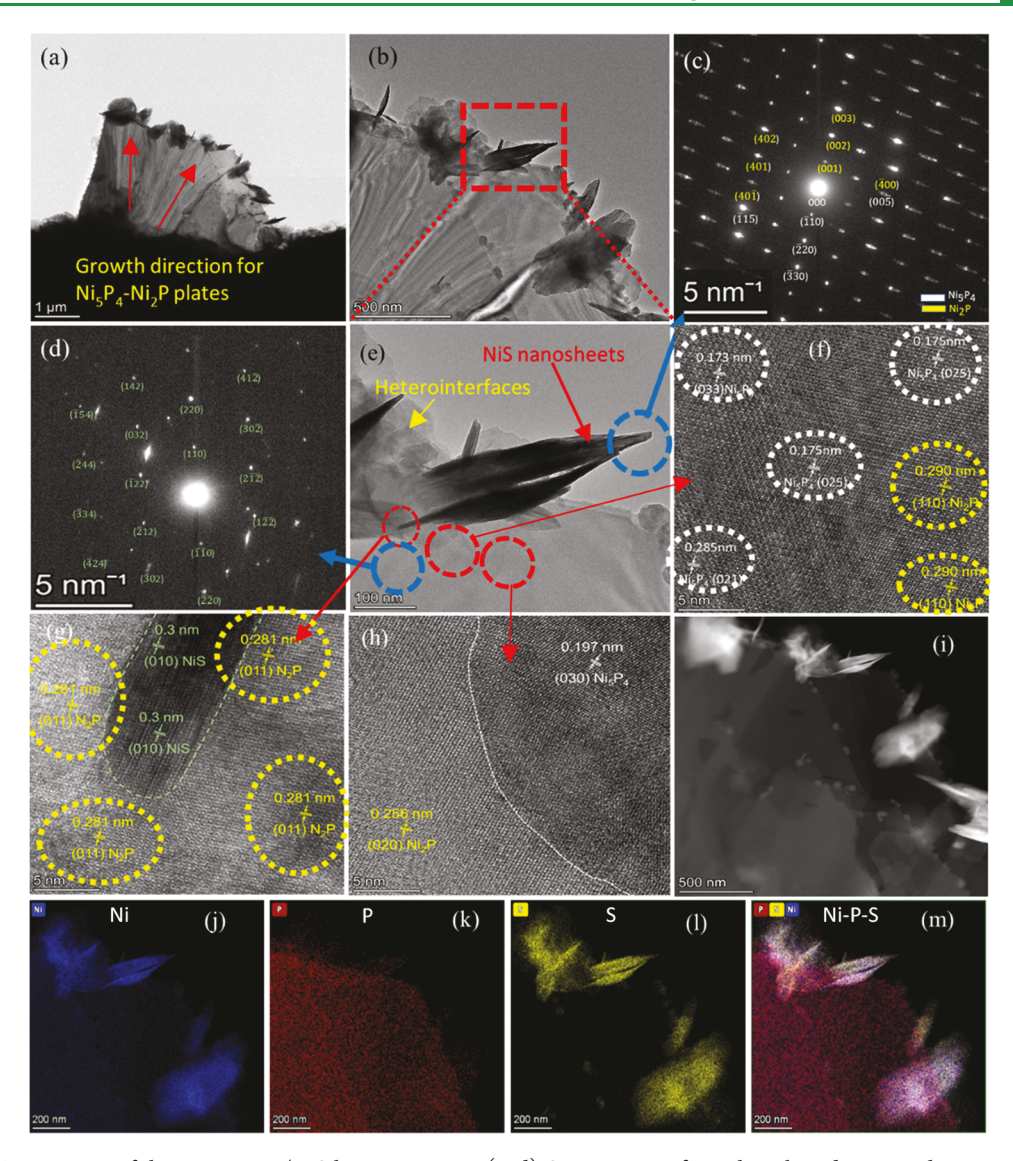


Figure 5. (a, b) TEM images of the  $Ni_5P_4$ - $Ni_2P/NiS$  heterostructure, (c, d) SAED images from the selected regions shown in (e). (e) Magnified TEM images, (f-h) HRTM images of the selected regions shown in (e), (i) dark-field STEM image, (j-m) corresponding EDS elemental mapping of Ni, P, S for the  $Ni_5P_4$ - $Ni_2P/NiS$  heterostructure.

the partial release of phosphorous during the sulfidation process at 300 °C and its combination with the present sulfur vapor at the surface. The narrow scan for the S 2p spectrum is deconvoluted to several peaks, shown in Figure 3d. Two peaks at 161.9 and 162.9 eV can be attributed to the S 2p<sub>3/2</sub>, and S 2p<sub>1/2</sub> orbitals of divalent sulfide ions (S<sup>2-</sup>) in Ni-S, which agrees well with the NiS spectrum reported earlier. The peak at 164 eV can be ascribed to the formation of S<sub>8</sub> during the vapor deposition treatment.

**B** Surface and Interface Morphology and Microstructure. The structure and surface morphology of the prepared catalysts are examined using scanning electron microscopy (SEM) and transition electron microscopy (TEM) to understand the effect of the sulfidation process. Images are taken from the Ni mesh (Figure S5) and after the phosphidation and sulfidation process (Figure 4). We realize that  $Ni_5P_4$  and  $Ni_2P$  phases cover the entire mesh surface after the phosphidation process, while  $Ni_5P_4$  is the dominant phase on the surface. As illustrated in Figure 4a,b, two surface features are noticeable, protrusions and vertically aligned plates, where protrusions encompass plates. Energy-dispersive

spectroscopy (EDS) analysis reveals that protrusions are Ni<sub>5</sub>P<sub>4</sub> phases (Figure S6). A broad view of nickel mesh after the phosphidation process is shown in Figure S6a to illustrate the uniform distribution of plates and protrusions over the mesh surface. The magnified SEM image in Figure 4b reveals that the vertically aligned plates adopt several steps throughout the facet surface or at the edges, while the overall thickness stays approximately below 100 nm, as displayed in Figure S6b. We postulate that these steps/shearlines form on the facets due to the extra strains derived from the synergistic presence of Ni<sub>5</sub>P<sub>4</sub> and Ni<sub>2</sub>P phases. Thus, these are called Ni<sub>5</sub>P<sub>4</sub>-Ni<sub>2</sub>P plates to highlight the simultaneous presence of both phases. Furthermore, we envisage that these steps/shearlines work as preferential sites with a lower barrier energy for initiating the growth of the epitaxial NiS nanosheets.<sup>27</sup> As displayed in Figure 4c,d, the population of the NiS nanosheets is the highest for NiPS3 electrocatalysts. EDS analyses are performed for two regions of A and B, as depicted in Figure 4e, where A and B are rich and scarce in sulfur, respectively (Figure S8). The EDS analyses indicate the formation of nickel sulfide in region A, while nickel phosphide is the dominant phase in

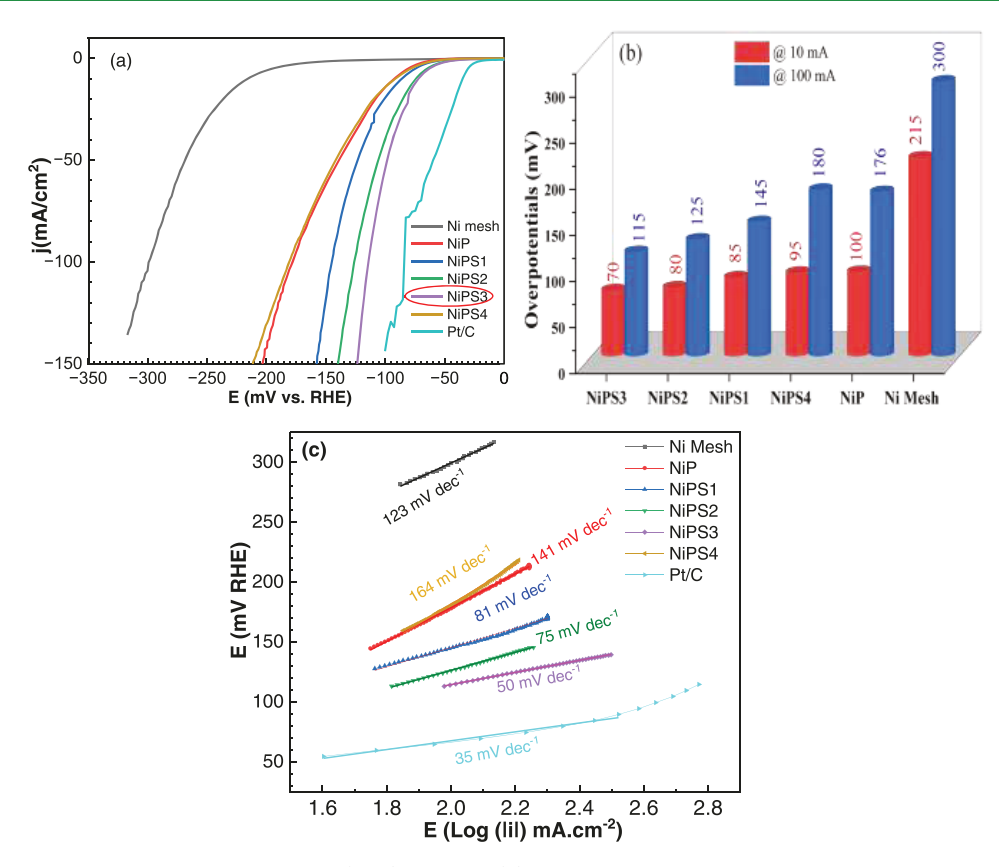


Figure 6. (a) IR-corrected linear sweep voltammetry (LSV) of HER, (b) overpotential profiles of the prepared catalysts, and (c) plot of Tafel slopes for the prepared catalysts.

region B. The atomic ratio of P/Ni in Figures S6d and S8b implies that Ni<sub>5</sub>P<sub>4</sub> is the dominant phase in vertically aligned plates before and after the sulfidation process, verified by the XRD and Rietveld analyses earlier. The EDS analysis in Figure S7 confirms the formation of Ni<sub>5</sub>P<sub>4</sub> as a dominant phase in the protrusion feature areas. The NiS nanosheets appear at the edges of the plates resembling the prickly pear fruits (Figure 4e,f), and Ni<sub>5</sub>P<sub>4</sub>-Ni<sub>2</sub>P plates represent the cactus leaves remarkably (Figure 4f). We discussed the formation of the prickly pear cactus in the schematic illustration shown in Figure 1a, where the primary nickel phosphide plates, Ni<sub>5</sub>P<sub>4</sub>-Ni<sub>2</sub>P, form during the phosphidation process, and the NiS nanosheets form during the sulfidation process.

TEM images in Figure 5 remarkably demonstrate the nanostructure features appearing after the joint phosphosulfidation process, where the NiS nanosheets start growing on the edge of Ni<sub>5</sub>P<sub>4</sub>-Ni<sub>2</sub>P plates. The TEM image in Figure 5a shows a broad view of a nickel phosphide plate accompanied by nickel sulfide nanosheets. As shown in Figure 5b,e, the sulfidation process generates heterogeneous interfaces because of the synergistic presence of different phases, particularly in the vicinity of the NiS roots, where the epitaxial NiS nanosheets initiate growing. These heterointerfaces can act as suitable regions for enhanced electron transfer and intensified electron exchangeability between catalytic sites and H\* species (H protons). As magnified in Figure 5e, the NiS nanosheets grow outward in random directions, and thereby, various crystallographic planes appear in the selected-area electron diffraction (SAED) pattern shown in Figure 5c. The SAED pattern obtained from the nanosheet's apex (the prickly pear fruit, Figure S9) confirms the formation of the hexagonal NiS

structure. By carefully investigating the SAED pattern (Figure 5d) collected from the Ni<sub>5</sub>P<sub>4</sub>-Ni<sub>2</sub>P plate (the cactus leaf), we observe a localized vibration at each shinning spot that can be attributed to the simultaneous diffraction from two hexagonal crystal structures corresponding to the Ni<sub>5</sub>P<sub>4</sub> and Ni<sub>2</sub>P phases.<sup>35</sup> It can be noted that many spots overlap in the diffraction pattern since the pattern is obtained from the contribution of both crystal structures. Thus, corresponding planes are identified for both phases. The simultaneous presence of several phases, including Ni<sub>5</sub>P<sub>4</sub>, Ni<sub>2</sub>P, and NiP<sub>2</sub> (semistable), was also reported by evaluating the SAED pattern corresponding to the synthesized nickel phosphide nanosheets.<sup>36</sup> The magnified TEM image shown in Figure 5e is used as a reference for further characterization. High-resolution TEM (HRTEM) images taken from red-marked circles regions near NiS nanosheets and its root are displayed in Figure 5f-h. As demonstrated in Figure 5f, the lattice fringes with a spacing of 0.290 nm are indicative of the interplanar spacing of (110) planes from the hexagonal Ni<sub>2</sub>P phase, while various lattice fringes with a spacing of 0.173, 0.175, and 0.285 can be related to the interplanar spacing of (033), (025), and (021) planes from the hexagonal Ni<sub>5</sub>P<sub>4</sub> phase, respectively. Indeed, the synergistic presence of both Ni<sub>5</sub>P<sub>4</sub> and Ni<sub>2</sub>P phases can also be realized from the HRTEM image in Figure 5f, representing the internal structural discontinuity in the Ni<sub>5</sub>P<sub>4</sub> phase due to a random distribution of the Ni<sub>2</sub>P phase marked by yellow circles.<sup>37</sup> This interference leads to the generation of Ni<sub>5</sub>P<sub>4</sub>/ Ni<sub>2</sub>P heterointerfaces at the nanoscale. Remarkably, the HRTEM image in Figure 5g confirms the formation of the epitaxial NiS nanosheets, where NiS ( $d_{(010)}$ = 0.300 nm) and  $Ni_2P$  ( $d_{(011)}$ = 0.281 nm) approximately share similar lattice

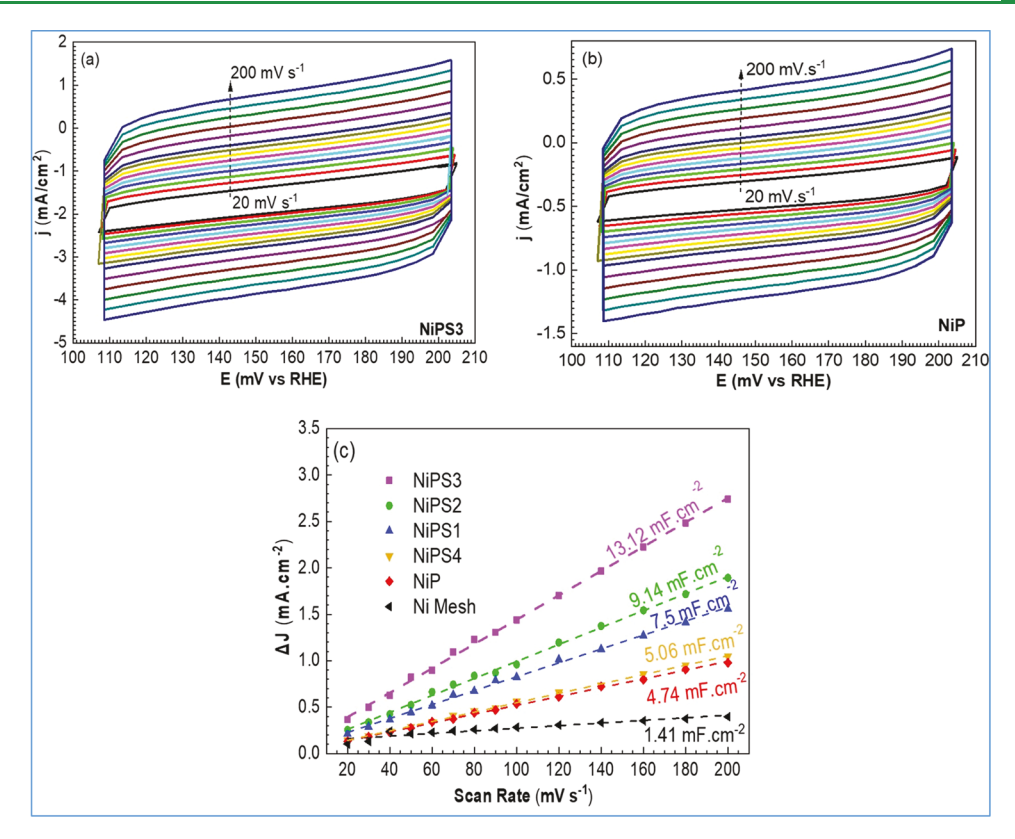


Figure 7. (a, b) cyclic voltammetry at scan rates from 20 to 200 mV s<sup>-1</sup> for NiPS3 and NiP, respectively, and (c) determination of  $C_{\rm dl}$  for all prepared catalysts.

distances, yielding to a decent d-spacing (interplanar space) matching between the  $Ni_2P$  phase and the epitaxial NiS phase.  $^{22,24,25}$ 

Therefore, the epitaxial interfacing between Ni<sub>2</sub>P and NiS crystals occurs along the (011) facets from Ni<sub>2</sub>P thanks to the negligible interfacial strain (Figure 1b). The dark-field scanning transmission electron microscopy (STEM) image also reveals the growth of NiS nanosheets from edges and the complex structure of the vertically grown Ni<sub>5</sub>P<sub>4</sub>-Ni<sub>2</sub>P plate (Figure 5i). The EDS mapping obtained under STEM mode reveals the uniform distribution of Ni and P in the vertically grown plates,<sup>38</sup> while Ni and S are only present in the epitaxial NiS nanosheets (Figure 5j,m). Considering these characterizations, we can verify emerging epitaxial interfaces between Ni<sub>2</sub>P and NiS phases at the nanoscale, which can facilitate electron transport during the electrocatalytic activity and strengthen the structure of the nanosheets. Figure S10a,b displays the Ni<sub>5</sub>P<sub>4</sub>-Ni<sub>2</sub>P/NiS structure in a magnified image. Figures S11 and S12 show TEM images and EDS analyses of the Ni<sub>5</sub>P<sub>4</sub> plate after the phosphidation process.

The implications of the structure-chemistry relationship in these Ni-P-S nanomaterials, as revealed by the XRD, SEM, TEM, and XPS analyses, can be described as follows. Note that the structural tuning of electrocatalysts has been recognized as one the most effective approaches to enhance interfacial interactions between electrocatalysts and electrolytes, leading to more significant HER performance. Specifically, one successful strategy is to judiciously grow epitaxial nanosheets out of the dominating phases, thereby expanding the active catalytic surface area and optimizing electronic features. It also tunes the energetics of intermediates via developing heterointerfaces. <sup>24,25</sup> This strategy eventually leads to more

significant hydrogen production and emphasizes the importance of using the conventional electrocatalyst as an appreciable substrate for constructing epitaxial nanosheets. Employing a sulfidation process leads to growing the epitaxial NiS nanosheets on the vertically aligned  $\rm Ni_5P_4\text{-}Ni_2P$  plates. Therefore, we expect our work to benefit from both simultaneous formation of  $\rm Ni_5P_4$  and  $\rm Ni_2P$  with nanodomain interfaces and the generation of the epitaxial NiS out of  $\rm Ni_2P$  phase. This unique 3D architecture resembles the prickly pear cactus. We provide detailed electrochemical studies to validate the effectiveness of these Ni–P–S nanostructures for enhanced HER performance.

C Electrochemical Characterization and HER Performance Evaluation. The electrocatalytic activities of the Ni<sub>5</sub>P<sub>4</sub>-Ni<sub>2</sub>P/NiS (plates/nanosheets) heterostructures are investigated specifically for the HER performance. We aim to determine the effect of the epitaxial NiS nanosheets and generated heterointerfaces in hydrogen production. The HER activities are evaluated using electrochemical measurements in Ar saturated 0.5 M H<sub>2</sub>SO<sub>4</sub> solution with a reference electrode of Ag/AgCl, calibrated to a reversible hydrogen electrode (RHE). We also use the normalized electrocatalytic current density by considering the catalysts' geometry and surface area. As shown in Figure 6a, the IR-corrected linear sweep voltammetry (LSV) at a scan rate of 5 mV s<sup>-1</sup> demonstrates that the epitaxial growth of NiS nanosheets can boost catalytic activities. In contrast, the NiP catalyst displays a lower HER activity. The NiPS3 electrocatalyst shows the lowest HER onset overpotential of 35 mV, which is a decent value compared to the commercial Pt/c electrode and lower than that of the NiP electrocatalyst (70 mV).<sup>30</sup> A noticeable feature related to the onset overpotential is that it is intrinsic to the

Table 1. Comparison of Various Ni-P-S Electrocatalyst Systems with Their HER Activity<sup>a,b</sup>

				HER activity			
source	preparation process	catalyst composition	solution	$\eta_{10}^{*}$	$\eta_{100}^{*}$	Tafel slope**	ref
NF	sulfo-phosphidation	NiS and Ni <sub>8</sub> P <sub>3</sub>	I	68.4	130	46.6	41
NF	one-step phospho-sulfidation	NiS, Ni <sub>2</sub> P <sub>2</sub> S <sub>6</sub>	I	140	210	72.8	42
NF	one-step electrodeposition	$Ni-NiSP_x$ (amorphous)	II	46	145	86	43
NF	hydrothermal + sulfo-plasma/phosphidation	$S_{vacancy}$ -Ni $_3S_{2-X}P_X$	I	89	169	122.5	44
NF	phospho-sulfidation	$NiP_{0.62}S_{0.38}$	I	52		52.3	17
NF	phospho-sulfidation	NiPS <sub>3</sub>	I	74	175	86	23
Ni <sub>5</sub> P <sub>4</sub> nanoplates	phospho-sulfidation of Ni(OH) <sub>2</sub> ·0.75H <sub>2</sub> O	$S_{doped}$ - $Ni_5P_4$	III	56	104	43.6	20
NiPS <sub>3</sub> bulk	electrochemical exfoliation of NiPS <sub>3</sub>	intercalated NiPS <sub>3</sub>	I	158		95	45
NiPS <sub>3</sub> particles	H <sub>2</sub> /Ar atmosphere + thermal treatment	NiPS <sub>3</sub> /Ni <sub>2</sub> P epitaxy	I	85		82	22
NiPS <sub>3</sub> bulk	ball-milling exfoliation of NiPS <sub>3</sub>	vacancy-NiPS <sub>3</sub>	I	126	200	65.4	46
NiPS <sub>3</sub> bulk	electrochemical exfoliation of NiPS <sub>3</sub>	thin NiPS <sub>3</sub> exfoliated layers	I	205		74	47
NF	hydrothermal + sulfo-phosphidation	$S_{doped}$ - $Ni_2P$	I	179	280	62	48
NF	phospho-sulfidation	Ni <sub>2</sub> P/Ni <sub>0.96</sub> S	IV	72	239	149	49
Ni mesh	phospho-sulfidation	Ni <sub>5</sub> P <sub>4</sub> -Ni <sub>2</sub> P/NiS	III	70	115	50	***

<sup>&</sup>lt;sup>a</sup>NF: Nickel foam, the current work is shown with \*\*\*, \*: mA cm<sup>-2</sup>, \*\*: mV dec<sup>-1</sup>, I: 1 M KOH, II: 1 M NaOH, III: 0.5 M H<sub>2</sub>SO<sub>4</sub>, IV: 1 M KOH and 0.5 M urea. <sup>b</sup>Phospho-sulfidation and sulfo-phosphidation are the two-step processes differing in order.

catalyst's surface properties regardless of its loading.2 For the HER performance, overpotentials at the current density of 10 and 100 mA cm<sup>-2</sup> are obtained from LSV curves and shown in Figure 6b. It reveals that the overpotential is significantly decreased for NiPS3 and other NiPS series. However, the NiP electrocatalyst contains the highest overpotentials. This noticeable catalytic activity confirms the importance of reinforcing intrinsic catalytic sites and expanding the active surface area by developing the epitaxial growth of NiS nanosheets upon the sulfidation process. Although the overpotential values for the NiPS3 electrode at the current densities of 10 and 100 mA cm<sup>-2</sup> (70 and 115 mV, respectively) do not surpass the catalytic performance of the Pt-group catalysts, this work demonstrates the importance of improving the electronic and structural features for boosting the electrocatalytic activity. 22,25 It is worth mentioning that the primary goal of the current study is not to introduce a champion electrocatalyst dominating the sophisticated Ptgroup catalysts. Further, it endows a new avenue for constructing seamless electrocatalysts. A linear fitting by the Tafel equation is performed on the polarization curves based on the method explained by Murthy et al.<sup>39</sup> Figure 6c shows the corresponding Tafel plots. Tafel slopes are inversely related to the charge transfer coefficient of HER, which directly demonstrates how efficiently electrons are exchanged across the interface. Tafel slopes also serve as indicators for controlling the mechanism of HER established across the interface. Noticeably, the Tafel slope profile for the Ni<sub>5</sub>P<sub>4</sub>-Ni<sub>2</sub>P/NiS heterostructure reflects a decreasing trend with increasing sulfur content during the sulfidation process, where NiPS3 shows the lowest slope (50 mV dec<sup>-1</sup>) compared to other catalysts, particularly NiP (141 mV dec-1). These findings indicate efficient kinetics of HER due to the emerging NiS nanosheets.

It is worth mentioning that estimating the turnover frequency (TOF), which is indicative of the number of transported electrons for each active site per second, is not feasible for the current study because determining the number of active sites for the complex heterostructures is cumbersome. Therefore, to construct a relation between the structural properties and active catalytic surface area of the electrocatalysts, we measure the double-layer capacitance ( $C_{\rm dl}$ ) from

the cyclic voltammetry (CV) curves in the limited cathodic range of 105-205 mV vs RHE (Figure 7a,b). The CV plots related to NiPS1, NiPS2, and NiPS4 are shown in Figure S13. The electrochemically active surface area (ECSA) is directly proportional to the  $C_{dl}$  ECSA =  $C_{dl}/C_s$  ( $C_s$  is the assumed specific capacitance), which is the linear slope of  $\Delta j$  as a function of a series of scan rates obtained from the CV curves. The measured  $C_{\rm dl}$  values are 13.12 and 4.74 mF cm<sup>-2</sup> for NiPS3 and NiP, respectively, indicating a nearly 3-fold higher ECSA for the electrocatalyst containing the epitaxial NiS nanosheets. The NiPS3 catalyst with the most significant C<sub>dl</sub> indicates that the HER activity proceeds with a more enhanced adsorption of H\* on the active sites compared to other prepared electrocatalysts. Thus, electron exchangeability improves considerably between the active sites and adsorbed protons from the electrolyte, remarkably enhancing HER performance for the NiPS3 electrocatalyst. The characterization already performed, like LSV and CV, reveals the superior HER performance of the NiPS3 electrocatalyst. SEM images in Figure 4c,d illustrate that increasing the sulfur content during the sulfidation process causes the population of NiS to rise on the Ni<sub>5</sub>P<sub>4</sub>-Ni<sub>2</sub>P plates. For the NiPS3 electrocatalyst, it is envisaged that the epitaxial NiS nanosheets can provide greater accommodation for adsorbed intermediates, and the interfacial interaction between the catalyst and intermediate species proceeds more efficiently. In addition, emerging abundant heterointerfaces may positively influence the catalytic activity. Therefore, the unique structure of Ni<sub>5</sub>P<sub>4</sub>-Ni<sub>2</sub>P/NiS (plates/nanosheets) can boost the HER performance compared to the other prepared catalysts.

Furthermore, LSV results also confirm that the NiPS3 electrocatalyst offers the lowest overpotentials and Tafel slopes. These significant improvements imply the catalytic activity is enhanced, and the NiPS3 electrocatalyst demands the lowest electrical energy and shows the quickest hydrogen evolution kinetics. The CV studies and measuring the capacitances, as shown in Figure 7a–c, reflect that the NiPS3 electrocatalyst retains the largest capacitance, which can be attributed to the emerging epitaxial NiS nanosheets. The generation of the epitaxial NiS nanosheets increases the active surface area that synergistically accommodates a higher number of H<sub>ad</sub> species and facilitates electron transition.<sup>40</sup>

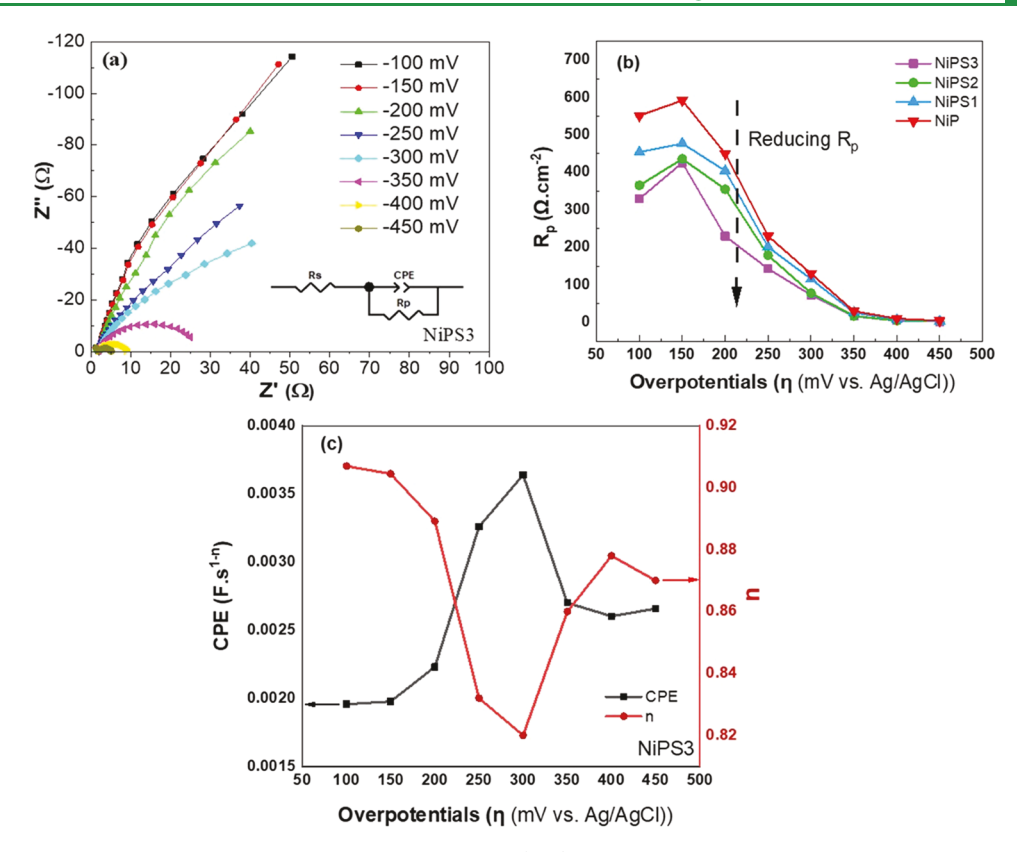


Figure 8. (a) Nyquist curves of electrochemical impedance spectroscopy (EIS) at overpotentials ranging from 100 to 450 mV, (b) charge transfer resistance (Rp) obtained from EIS data, and (c) CPE and n profiles obtained from NiPS3 for different overpotentials.

Furthermore, the following EIS results also show that the interface between NiPS3 and electrolyte establishes the lowest charge transfer resistance, indicating an accelerated electron transfer occurs at interfaces. Thus, in the conglomeration of the extensive studies with respect to the superiority of NiPS3, our evaluation suggests that the significant improvement in the catalytic performance of NiPS3 can be related to the growth of epitaxial NiS nanosheets compared to the other prepared catalysts.

To further understand the significance of the ternary nanostructured materials developed in this work and to elevate the technical approach used to synthesize such tailor-made prickly pears heterostructures, we compare our data with those reported in the literature. Table 1 represents electrocatalysts developed based on the ternary Ni-P-S system. The data presented in Table 1 demonstrates the significance of the current work compared to those already reported in the

As mentioned, this study does not present a champion electrocatalyst beating the current Pt bench market. However, it presents a new structure that has not been reported in the literature as shown in Tables 1 and S2. Noticeably, all studies on the Ni-P-S ternary systems can be categorized into 4 groups based on the catalysts' compositions, as follows:

- (i) Producing intermediate nickel phosphosulfide compositions, like  $NiP_xS_{1-x}$  refs 17 43 44, and 49.
- (ii) Producing sulfur-doped nickel phosphide or phosphordoped nickel sulfide, refs 20 48,.
- (iii) Producing stoichiometric compounds, like NiPS<sub>3</sub>, NiS, and Ni<sub>8</sub>P<sub>3</sub>, and using further procedures such as ballmilling or electrochemical processes to exfoliate thin layers, refs 23 41 42, 45-47,.

(iv) Generating the in situ epitaxial Ni<sub>2</sub>P nanodomains on 2D NiPS<sub>3</sub> nanosheets, ref 22.

Thus, the presented comparison reiterates the novelty of the current study, in which a seamless 3D electrocatalyst is synthesized using sequential phase alterations on an ultrathin nickel mesh. The importance of the synthesized nanostructure relies on the epitaxial growth of NiS nanosheets out of the Ni<sub>2</sub>P phase and, consequently, the formation of heterointerfaces near its nucleation sites.

Furthermore, to gain broader insights into the kinetics of the catalytic activity during HER catalysis, we use electrochemical impedance spectroscopy (EIS) techniques over a range of applied overpotentials from -100 to -450 mV vs Ag/AgCl. In fact, assessing the catalytic activity at constant overpotentials beyond the onset potentials is a convenient method for comparing the electronic characters and the importance of structural development. 50 Anantharaj and Noda realized that a rational correlation could be found for the charge transfer resistances at the constant potentials in the catalytic turnover regions, in which the entire interface could be subjected to electrocatalytic activities.<sup>51</sup> Evaluating EIS responses as a function of applied overpotentials can also shed light on the role of heterointerfaces generated owing to the epitaxial growth. The Nyquist plot of EIS data for the NiPS3 electrocatalyst is demonstrated in Figure 8a. It exhibits a depressed semicircle for all studied potentials, indicating the HER activity can be characterized by one time constant and only controlled by the charge transfer kinetics throughout the studied frequencies.<sup>52</sup> The experimental data are fitted using the equivalent circuit shown in Figure 7a. R<sub>s</sub> represents the ohmic resistance imposed by all connections and the electrolyte.  $R_p$  and CPE elements indicate the polarization

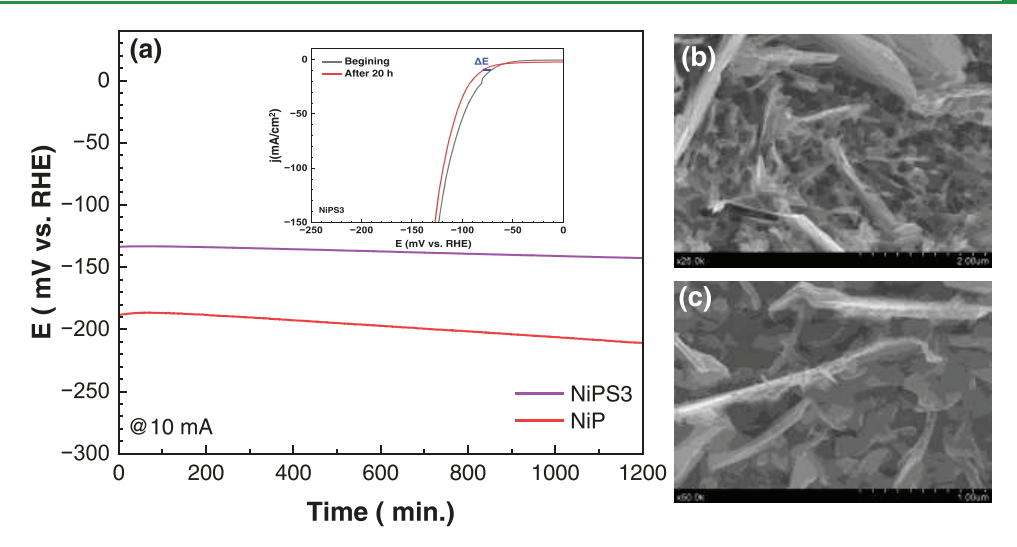


Figure 9. (a) Chronopotentiometry plot of HER activity at 10 mA for 20 h with the intersection of LSV plot related to before and after 20 h stability test. (b, c) SEM images related to NiP and NiPS3 electrodes after 20 h catalytic activity.

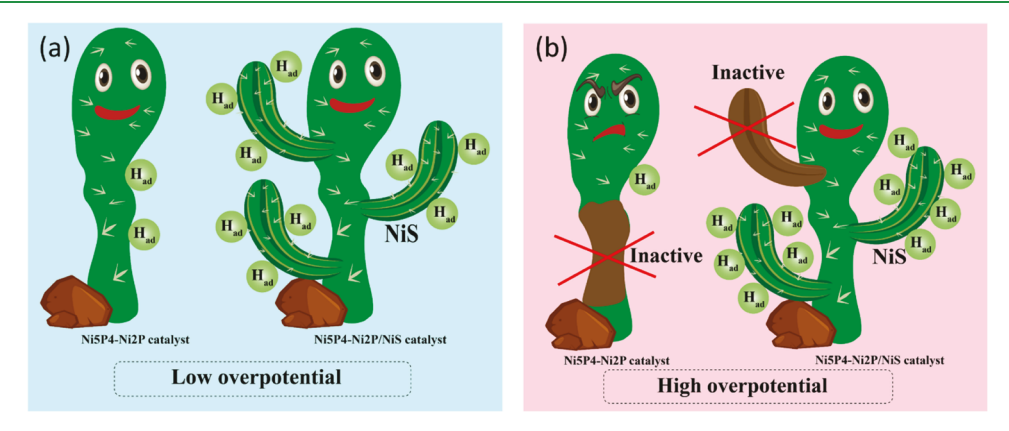


Figure 10. Cartoon representing the behavior of NiP and NiPS electrocatalysts during HER performance for low overpotentials (<-300 mV vs Ag/AgCl) and high overpotentials (>-300 mV).

resistance and the pseudo-capacitance arising from the charge transfer at the interface between active catalytic sites and adsorbed protons.<sup>53</sup> The CPE is used instead of the capacitance element due to depressed semicircles in Nyquist graphs. As shown in Figure 8b, the  $R_p$  reduces with applied potentials, in which the NiPS3 electrocatalyst demonstrates the lowest charge resistance at each potential, indicating a facilitated H\* adsorption on the active catalytic sites. 53 Thus, we realize the electron exchangeability is significantly enhanced for the electrocatalyst containing the largest population of the epitaxial NiS nanosheets, thanks to the largest ECSA and its higher intrinsic catalytic sites compared to other catalysts. On the other hand, the NiP catalyst consisting of the Ni<sub>5</sub>P<sub>4</sub>-Ni<sub>2</sub>P composition demonstrates the lowest electron transfer rate, leading to the weakest HER performance. Indeed, we realize a direct relation exists between raising the ECSA and decreasing the  $R_p$  trend. The measured  $R_p$  for the NiPS3 electrode shows the minimum resistance at each applied potential, implying that the transferring electrons to the adsorbed H\* species proceed with accelerated reaction kinetics during the HER performance.<sup>54</sup> These results confirm that the generated epitaxial interfaces and heterointerfaces significantly influence the HER performance. Indeed, the generation of the epitaxial NiS nanosheets lowers the charge transport resistance at the interfaces between Ni<sub>2</sub>P and NiS phases and reinforces the

electron transfer rate to the adsorbed H\*.<sup>22</sup> Further, the heterostructures emerging near the NiS nanosheets add to the structural and electronic improvements. These results are consistent with the overpotentials and Tafel slopes obtained for the electrocatalysts shown in Figure 6b,c.

The impedance of CPE can be expressed as

$$Z_{\text{CPE}} = A(j\omega)^{-n} \tag{1}$$

where  $A = 1/C_n$  and n = 1 (in the absence of frequency dispersion). It can be added that n is related to the surface condition of the electrocatalyst at different overpotentials. It is also utilized to alter the CPE to a pure capacity, where the closer to 1, the more the capacitance behavior can appear. Indeed, it is believed that n varies with the homogeneous distribution of active catalytic sites.<sup>55</sup> As shown in Figure 8c, we understand that the distribution of active sites varies with the applied overpotentials over the catalyst's surface, in which the homogeneity reduces with the applied potentials indicating that the number of active catalytic sites depletes and then mitigates at higher overpotentials (above 300 mV). In contrast, the CPE, representing the pseudo-capacitance of the formed double layer, increases with the applied potential until 300 mV, implying that the electron exchangeability rate over the active catalytic sites increases and then slightly reduces. Thus, it can be deduced that though the number of active sites is depleted,

the activity of the remaining sites is intensified with the applied overpotential. The durability of NiP and NiPS3 electrodes is evaluated for 20 h and demonstrated by a chronopotentiometry plot for the cathodic potential of 10 mA. The data are shown in Figure 9. As apparent, the voltage change for NiPS3 catalysts is negligible, and the change of overpotential is also insignificant, which can be confirmed by the intersection LSV plot regarding NiPS3 electrode. However, the voltage increased during HER activity for the NiP electrocatalyst, indicating some surface deterioration. Noticeably, the SEM image from the surface of the NiP electrode after 20 h shows the impact of catalytic activity in the forms of pits, while the surface of the NiPS3 electrode could sustain efficiently. The surface for NiPS3 catalysts does not show any pitting effect, and the structure could preserve some of the NiS nanosheets even after 20 h of HER activity.

Figure 10 illustrates the difference in the behavior of NiP and NiPS electrocatalysts in a range of reducing overpotentials. The cartoon explains that the ternary system provides a larger active catalytic surface area compared to the nickel phosphide catalyst while working at low overpotentials (<-300 mV vs Ag/AgCl). After switching to high overpotentials, although some areas of the ternary NiPS system become inactive, those active catalytic areas accommodate a higher number of H<sub>ad</sub> as an indication of compensating for inactive catalytic areas.

Taking into account the obtained results, we suggest the significant improvement observed for the catalytic activity of the Ni<sub>5</sub>P<sub>4</sub>-Ni<sub>2</sub>P/NiS (plates/nanosheets) stems mainly from expanding ECSA because of growing the epitaxial NiS nanosheets and strengthening the intrinsic catalytic activity due to the generated heterointerfaces. We realize that the epitaxially grown nanosheets and heterointerface stabilize more significant H\* adsorption over the active catalytic sites because of supporting the greater active surface area.<sup>22</sup>

The fundamental goal of the Ni-P-S ternary electrocatalytic system is to enhance electron transfer to adsorbed H\* species. Generally, the HER activity can be optimized by enhancing the intrinsic catalytic activity or increasing the number of exposed active catalytic sites. The heterointerfaces chemically include a nanoscale mixture of various phases formed during the phosphidation and sulfidation procedures. Therefore, the catalytic activity of heterointerfaces may achieve the goal of hitting two birds with one stone, namely, enhancing the intrinsic catalytic activity by containing nanoscale defects and expanding the active surface areas simultaneously. In fact, introducing defects through creating heterointerfaces is an effective strategy to improve the catalytic activity, which may consequently modulate the electronic structure of the interface by reducing the adsorption-free energy of H\* species during the HER performance.<sup>56</sup> In addition, the heterointerfaces inherit a synergistic effect of different components, where the unique structure of the heterointerfaces can provide stronger affinity with H\* species and thus improve HER catalytic activity.5

The heterointerfaces are generated near the epitaxial NiS nanosheets, as evidenced in the structure and morphology characterizations. Thus, these heterostructures benefit from a long-range disordered structure and abundant defects in correspondence with the compositional and structural variation. Another critical factor, although there are only limited studies/reports available at this time, is the chemistry of epitaxial interfaces that facilitates the enhanced catalytic activity for HER. Teng et al. reported significant improvement

in the catalytic activity of hydrogen reduction due to the generation of abundant active sites via the formation of the heterogeneous structure.<sup>58</sup> Liu et al. also reported synthesizing a heterointerface between Ni<sub>2</sub>P-NiP<sub>2</sub> as a successful strategy for establishing strong electronic coupling effects between various phases.<sup>59</sup> They showed electrons could transfer from P to Ni at the heterointerfaces, thereby reducing the adsorption energy of H\* species. Thus, our understanding is that the nanoscale mixture of nickel phosphosulfide in the heterointerfaces optimizes the intermediate hydrogen binding energy. To conclude that the chemically tailored heterointerfaces resulting from the mixture of different phases formed during the phosphidation and sulfidation procedures, where a controlled process dictates the chemistry of such interfaces formed, are the key to promoting the generation of abundant active sites, which in turn result in enhanced HER performance of the electrocatalysts designed in this work.

#### CONCLUSIONS

Herein, we demonstrate a controllable phospho-sulfidation process to synthesize the Ni<sub>5</sub>P<sub>4</sub>-Ni<sub>2</sub>P/NiS (plates/nanosheets) electrocatalyst with abundant epitaxial heterointerfaces for hydrogen production. A regional prickly pear cactus with plentiful surface area motivates this study to design a synthesis strategy that led to the construction of a 3D heterostructure electrocatalyst with an abundant active catalytic area and enhanced intrinsic catalytic activity. We rationally employ an ultrathin nickel mesh to facilitate a uniform phase transformation and support spatial freedom for departing produced hydrogen. After the phosphidation process, the Ni<sub>5</sub>P<sub>4</sub> and Ni<sub>2</sub>P structures, known for their outstanding HER performance, form simultaneously on the mesh surface with two surface features, protrusions and vertically aligned plates. We realize that Ni<sub>5</sub>P<sub>4</sub> and Ni<sub>2</sub>P phases coexist in the vertical plates, making nanoscale heterointerfaces and reinforcing electrical connectivity. After the sulfidation process, the epitaxial NiS nanosheets nucleate and grow primarily at the edges, kinks, or steps observed on the facets of the Ni<sub>5</sub>P<sub>4</sub>-Ni<sub>2</sub>P plates. The in situ epitaxial interfaces nucleate at the root of the NiS nanosheets interfacing with the Ni<sub>2</sub>P phase and induce the heterointerfaces formation. We deduce that the electrochemical surface area (ECSA) expansion and intrinsic catalytic activity enhancement are the two influential factors optimizing the Ni<sub>5</sub>P<sub>4</sub>-Ni<sub>2</sub>P/NiS electrocatalytic performance. The electrochemical studies, including EIS and CV analyses, verify the importance of emerging heterostructures in reinforcing electron mobility and stability at higher overpotentials. Our findings emphasize the importance of the successful growth of epitaxial nanosheets in improving electrocatalytic activities of the Ni<sub>5</sub>P<sub>4</sub>-Ni<sub>2</sub>P/NiS heterostructures.

## ASSOCIATED CONTENT

# Supporting Information

The Supporting Information is available free of charge at https://pubs.acs.org/doi/10.1021/acsami.3c00781.

Materials characterization, electrochemical characterization, and figures; controlled process employed for the synthesis of Ni–P–S heteroepitaxial electrocatalysts; and approach adopted, materials characterization, electrochemical characterization, and additional figures (in support of claims made) (PDF)

#### AUTHOR INFORMATION

## **Corresponding Author**

C. V. Ramana — Centre for Advanced Materials Research (CMR), University of Texas at El Paso, El Paso, Texas 79968, United States; Department of Mechanical Engineering, University of Texas at El Paso, El Paso, Texas 79968, United States; orcid.org/0000-0002-5286-3065; Email: rychintalapalle@utep.edu

#### **Authors**

- Navid Attarzadeh Centre for Advanced Materials Research (CMR), University of Texas at El Paso, El Paso, Texas 79968, United States; Environmental Science and Engineering, University of Texas at El Paso, El Paso, Texas 79968, United States
- Debabrata Das Centre for Advanced Materials Research (CMR), University of Texas at El Paso, El Paso, Texas 79968, United States; Occid.org/0000-0003-4326-6805
- Srija N. Chintalapalle Centre for Advanced Materials Research (CMR), University of Texas at El Paso, El Paso, Texas 79968, United States
- Susheng Tan Department of Electrical and Computer Engineering, Petersen Institute of NanoScience and Engineering, University of Pittsburg, Pittsburgh, Pennsylvania 15261, United States; orcid.org/0000-0002-6162-7443
- V. Shutthanandan Environmental Molecular Sciences Laboratory (EMSL), Pacific Northwest National Laboratory (PNNL), Richland, Washington 99352, United States; orcid.org/0000-0003-2957-7535

Complete contact information is available at: https://pubs.acs.org/10.1021/acsami.3c00781

#### Notes

The authors declare no competing financial interest.

# ■ ACKNOWLEDGMENTS

The authors acknowledge, with pleasure, support from the National Science Foundation (NSF) with NSF-PREM grant #DMR-1827745. A portion of this research (Chemical Composition Analyses using X-ray Photoelectron Spectroscopy) was performed on a project award (10.46936/cpcy-proj.2021.60259/60008213) from the Environmental Molecular Sciences Laboratory, a DOE Office of Science User Facility sponsored by the Biological and Environmental Research program under Contract No. DE-AC05-76RL01830 and also funded in part by a grant from the Washington State Department of Commerce's Clean Energy Fund.

#### REFERENCES

- (1) de Luna, P.; Hahn, C.; Higgins, D.; Jaffer, S. A.; Jaramillo, T. F.; Sargent, E. H. What Would It Take for Renewably Powered Electrosynthesis to Displace Petrochemical Processes? *Science* **2019**, 364, No. e.aav3506.
- (2) Anantharaj, S.; Noda, S.; Jothi, V. R.; Yi, S. C.; Driess, M.; Menezes, P. W. Strategies and Perspectives to Catch the Missing Pieces in Energy-Efficient Hydrogen Evolution Reaction in Alkaline Media. *Angew. Chem., Int. Ed.* **2021**, *60*, 18981–19006.
- (3) Yin, H.; Zhao, S.; Zhao, K.; Muqsit, A.; Tang, H.; Chang, L.; Zhao, H.; Gao, Y.; Tang, Z. Ultrathin Platinum Nanowires Grown on Single-Layered Nickel Hydroxide with High Hydrogen Evolution Activity. *Nat. Commun.* **2015**, *6*, No. 6430.
- (4) Sun, M.; Liu, H.; Qu, J.; Li, J. Earth-Rich Transition Metal Phosphide for Energy Conversion and Storage. *Adv. Energy Mater.* **2016**, *6*, No. 1600087.

- (5) Tang, C.; Zhang, R.; Lu, W.; He, L.; Jiang, X.; Asiri, A. M.; Sun, X. Fe-Doped CoP Nanoarray: A Monolithic Multifunctional Catalyst for Highly Efficient Hydrogen Generation. *Adv. Mater.* **2017**, *29*, No. 1602441.
- (6) Liu, T.; Xie, L.; Yang, J.; Kong, R.; Du, G.; Asiri, A. M.; Sun, X.; Chen, L. Self-Standing CoP Nanosheets Array: A Three-Dimensional Bifunctional Catalyst Electrode for Overall Water Splitting in Both Neutral and Alkaline Media. *ChemElectroChem* **2017**, *4*, 1840–1845.
- (7) Cabán-Acevedo, M.; Stone, M. L.; Schmidt, J. R.; Thomas, J. G.; Ding, Q.; Chang, H. C.; Tsai, M. L.; He, H.; Jin, S. Efficient Hydrogen Evolution Catalysis Using Ternary Pyrite-Type Cobalt Phosphosulphide. *Nat. Mater.* **2015**, *14*, 1245–1251.
- (8) Liu, W.; Hu, E.; Jiang, H.; Xiang, Y.; Weng, Z.; Li, M.; Fan, Q.; Yu, X.; Altman, E. I.; Wang, H. A Highly Active and Stable Hydrogen Evolution Catalyst Based on Pyrite-Structured Cobalt Phosphosulfide. *Nat. Commun.* **2016**, *7*, No. 10771.
- (9) Wu, Z.; Li, X.; Liu, W.; Zhong, Y.; Gan, Q.; Li, X.; Wang, H. Materials Chemistry of Iron Phosphosulfide Nanoparticles: Synthesis, Solid State Chemistry, Surface Structure, and Electrocatalysis for the Hydrogen Evolution Reaction. *ACS Catal* **2017**, *7*, 4026–4032.
- (10) Bae, S.-H.; Kim, J.-E.; Randriamahazaka, H.; Moon, S.-Y.; Park, J.-Y.; Oh, I.-K. Seamlessly Conductive 3D Nanoarchitecture of Core—Shell Ni-Co Nanowire Network for Highly Efficient Oxygen Evolution. *Adv. Energy Mater.* **2017**, *7*, No. 1601492.
- (11) Zhang, H.; Maijenburg, A. W.; Li, X.; Schweizer, S. L.; Wehrspohn, R. B. Bifunctional Heterostructured Transition Metal Phosphides for Efficient Electrochemical Water Splitting. *Adv. Funct. Mater.* **2020**, *30*, No. 2003261.
- (12) Ye, R.; del Angel-Vicente, P.; Liu, Y.; Arellano-Jimenez, M. J.; Peng, Z.; Wang, T.; Li, Y.; Yakobson, B. I.; Wei, S. H.; Yacaman, M. J.; Tour, J. M. High-Performance Hydrogen Evolution from  $MoS_{2(1-x)}P$  Solid Solution. *Adv. Mater.* **2016**, *28*, 1427–1432.
- (13) Attarzadeh, N.; Nuggehalli, R.; Ramana, C. V. Application of Transition Metal Phosphides to Electrocatalysis: An Overview. *JOM* **2022**, *74*, 381–395.
- (14) Shi, Y.; Zhang, B. Recent Advances in Transition Metal Phosphide Nanomaterials: Synthesis and Applications in Hydrogen Evolution Reaction. *Chem. Soc. Rev.* **2016**, *45*, 1529–1541.
- (15) Liu, Y.; Vijayakumar, P.; Liu, Q.; Sakthivel, T.; Chen, F.; Dai, Z. Shining Light on Anion-Mixed Nanocatalysts for Efficient Water Electrolysis: Fundamentals, Progress, and Perspectives. *Nano-Micro Lett.* 2022, 14, No. 43.
- (16) Song, B.; Li, K.; Yin, Y.; Wu, T.; Dang, L.; Cabán-Acevedo, M.; Han, J.; Gao, T.; Wang, X.; Zhang, Z.; Schmidt, J. R.; Xu, P.; Jin, S. Tuning Mixed Nickel Iron Phosphosulfide Nanosheet Electrocatalysts for Enhanced Hydrogen and Oxygen Evolution. *ACS Catal.* **2017**, *7*, 8549–8557.
- (17) Luo, J.; Wang, H.; Su, G.; Tang, Y.; Liu, H.; Tian, F.; Li, D. Self-Supported Nickel Phosphosulphide Nanosheets for Highly Efficient and Stable Overall Water Splitting. *J. Mater. Chem. A* **2017**, *5*, 14865–14872.
- (18) Dai, Z.; Geng, H.; Wang, J.; Luo, Y.; Li, B.; Zong, Y.; Yang, J.; Guo, Y.; Zheng, Y.; Wang, X.; Yan, Q. Hexagonal-Phase Cobalt Monophosphosulfide for Highly Efficient Overall Water Splitting. *ACS Nano* **2017**, *11*, 11031–11040.
- (19) Kibsgaard, J.; Jaramillo, T. F. Molybdenum Phosphosulfide: An Active, Acid-Stable, Earth-Abundant Catalyst for the Hydrogen Evolution Reaction. *Angew. Chem., Int. Ed.* **2014**, *53*, 14433–14437.
- (20) Chang, J.; Li, K.; Wu, Z.; Ge, J.; Liu, C.; Xing, W. Sulfur-Doped Nickel Phosphide Nanoplates Arrays: A Monolithic Electrocatalyst for Efficient Hydrogen Evolution Reactions. *ACS Appl. Mater. Interfaces* **2018**, *10*, 26303–26311.
- (21) Wang, J.; Li, X.; Wei, B.; Sun, R.; Yu, W.; Ying Hoh, H.; Xu, H.; Li, J.; Ge, X.; Chen, Z.; Su, C.; Wang, Z. Activating Basal Planes of NiPS3 for Hydrogen Evolution by Nonmetal Heteroatom Doping. *Adv. Funct. Mater.* **2020**, *30*, No. 1908708.
- (22) Liang, Q.; Zhong, L.; Du, C.; Luo, Y.; Zhao, J.; Zheng, Y.; Xu, J.; Ma, J.; Liu, C.; Li, S.; Yan, Q. Interfacing Epitaxial Dinickel

- Phosphide to 2D Nickel Thiophosphate Nanosheets for Boosting Electrocatalytic Water Splitting. ACS Nano 2019, 13, 7975–7984.
- (23) Fang, L.; Xie, Y.; Guo, P.; Zhu, J.; Xiao, S.; Sun, S.; Zi, W.; Zhao, H. In Situ Formation of Highly Exposed NiPS<sub>3</sub> Nanosheets on Nickel Foam as an Efficient 3D Electrocatalyst for Overall Water Splitting. Sustainable Energy Fuels 2021, 5, 2537–2544.
- (24) Zhu, C.; Wang, A.-L.; Xiao, W.; Chao, D.; Zhang, X.; Tiep, N. H.; Chen, S.; Kang, J.; Wang, X.; Ding, J.; Wang, J.; Zhang, H.; Fan, H. J. In Situ Grown Epitaxial Heterojunction Exhibits High-Performance Electrocatalytic Water Splitting. *Adv. Mater.* **2018**, *30*, No. 1705516.
- (25) An, L.; Feng, J.; Zhang, Y.; Wang, R.; Liu, H.; Wang, G.-C.; Cheng, F.; Xi, P. Epitaxial Heterogeneous Interfaces on N-NiMoO $_4$ /NiS $_2$  Nanowires/Nanosheets to Boost Hydrogen and Oxygen Production for Overall Water Splitting. *Adv. Funct. Mater.* **2019**, 29, No. 1805298.
- (26) Marghussian, V. Glass Crystallization. In *Nano-Glass Ceramics Processing, Properties and Applications*; Marghussian, V., Ed.; William Andrew Publishing, 2015; pp 1–62 DOI: 10.1016/b978-0-323-35386-1.00001-3.
- (27) Habelitz, S.; Höche, T.; Hergt, R.; Carl, G.; Rüssel, C. Microstructural Design through Epitaxial Growth in Extruded Mica Glass-Ceramics. *Acta Mater.* **1999**, *47*, 2831–2840.
- (28) Halim, J.; Kota, S.; Lukatskaya, M. R.; Naguib, M.; Zhao, M.-Q.; Moon, E. J.; Pitock, J.; Nanda, J.; May, S. J.; Gogotsi, Y.; Barsoum, M. W. Synthesis and Characterization of 2D Molybdenum Carbide (MXene). *Adv. Funct. Mater.* **2016**, *26*, 3118–3127.
- (29) Wang, X.; Kolen'Ko, Y. V.; Bao, X. Q.; Kovnir, K.; Liu, L. One-Step Synthesis of Self-Supported Nickel Phosphide Nanosheet Array Cathodes for Efficient Electrocatalytic Hydrogen Generation. *Angew. Chem., Int. Ed.* **2015**, *54*, 8188–8192.
- (30) Liu, S.; Hu, C.; Lv, C.; Cai, J.; Duan, M.; Luo, J.; Song, J.; Shi, Y.; Chen, C.; Luo, D.; Watanabe, A.; Aoyagi, E.; Ito, S. Facile Preparation of Large-Area Self-Supported Porous Nickel Phosphide Nanosheets for Efficient Electrocatalytic Hydrogen Evolution. *Int. J. Hydrogen Energy* **2019**, *44*, 17974–17984.
- (31) Ramana, C. V.; Roy, S.; Zade, V.; Battu, A. K.; Makeswaran, N.; Shutthanandan, V. Electronic Structure and Chemical Bonding in Transition-Metal-Mixed Gallium Oxide (Ga2O3) Compounds. *J. Phys. Chem. Solids* **2021**, *157*, No. 110174.
- (32) Ramana, C. V.; Bandi, M.; N Nair, A.; Manciu, F. S.; Sreenivasan, S.; Shutthanandan, V. Electronic Structure, Chemical Bonding, and Electrocatalytic Activity of Ba(Fe $_{0.7}$ Ta $_{0.3}$ )O $_{3-\delta}$  Compounds. ACS Appl. Energy Mater. 2021, 4, 1313–1322.
- (33) Sun, H.; Xu, X.; Yan, Z.; Chen, X.; Cheng, F.; Weiss, P. S.; Chen, J. Porous Multishelled Ni<sub>2</sub>P Hollow Microspheres as an Active Electrocatalyst for Hydrogen and Oxygen Evolution. *Chem. Mater.* **2017**, 29, 8539–8547.
- (34) Qin, Z.; Chen, Y.; Huang, Z.; Su, J.; Diao, Z.; Guo, L. Composition-Dependent Catalytic Activities of Noble-Metal-Free NiS/Ni $_3$ S $_4$  for Hydrogen Evolution Reaction. *J. Phys. Chem. C* **2016**, 120, 14581–14589.
- (35) Danielsen, H. K.; Hald, J.; Grumsen, F. B.; Somers, M. A. J. On the Crystal Structure Of Z-Phase Cr(V,Nb)N. *Metall. Mater. Trans. A* **2006**, *37*, 2633–2640.
- (36) Hu, C.; Cai, J.; Liu, S.; Lv, C.; Luo, J.; Duan, M.; Chen, C.; Shi, Y.; Song, J.; Zhang, Z.; Watanabe, A.; Aoyagi, E.; Ito, S. General Strategy for Preparation of Porous Nickel Phosphide Nanosheets on Arbitrary Substrates toward Efficient Hydrogen Generation. ACS Appl. Energy Mater. 2020, 3, 1036–1045.
- (37) Makeswaran, N.; Das, D.; Zade, V.; Gaurav, P.; Shutthanandan, V.; Tan, S.; Ramana, C. V. Size- and Phase-Controlled Nanometer-Thick  $\beta$ -Ga<sub>2</sub>O<sub>3</sub> Films with Green Photoluminescence for Optoelectronic Applications. *ACS Appl. Nano Mater.* **2021**, *4*, 3331–3338.
- (38) Ramana, C. V.; Ait-Salah, A.; Utsunomiya, S.; Backer, U.; Mauger, A.; Gendron, F.; Julien, C. M. Structural Characteristics of Lithium Nickel Phosphate Studied Using Analytical Electron Microscopy and Raman Spectroscopy. *Chem. Mater.* **2006**, *18*, 3788–3794.

- (39) Murthy, A. P.; Theerthagiri, J.; Madhavan, J. Insights on Tafel Constant in the Analysis of Hydrogen Evolution Reaction. *J. Phys. Chem. C* 2018, 122, 23943–23949.
- (40) Yin, Y.; Zhang, Y.; Gao, T.; Yao, T.; Zhang, X.; Han, J.; Wang, X.; Zhang, Z.; Xu, P.; Zhang, P.; Cao, X.; Song, B.; Jin, S. Synergistic Phase and Disorder Engineering in 1T-MoSe<sub>2</sub> Nanosheets for Enhanced Hydrogen-Evolution Reaction. *Adv. Mater.* **2017**, *29*, No. 1700311.
- (41) Duan, J.; Chen, S.; Zhao, C. Strained Nickel Phosphide Nanosheet Array. ACS Appl. Mater. Interfaces 2018, 10, 30029–30034
- (42) Zhang, X.; Zhang, S.; Li, J.; Wang, E. One-Step Synthesis of Well-Structured NiS–Ni $_2$ P $_2$ S $_6$  Nanosheets on Nickel Foam for Efficient Overall Water Splitting. *J. Mater. Chem. A* **2017**, *S*, 22131–22136.
- (43) Chen, X.; Li, Q.; Che, Q.; Chen, Y.; Tan, Y.; Xu, X. Self-Supported Ni/NiSP<sub>x</sub> Microdendrite Structure for Highly Efficient and Stable Overall Water Splitting in Simulated Industrial Environment. ACS Sustainable Chem. Eng. 2019, 7, 11778–11786.
- (44) Yang, Y.; Mao, H.; Ning, R.; Zhao, X.; Zheng, X.; Sui, J.; Cai, W. Ar Plasma-Assisted P-Doped Ni<sub>3</sub>S<sub>2</sub> with S Vacancies for Efficient Electrocatalytic Water Splitting. *Dalton Trans.* **2021**, *50*, 2007–2013.
- (45) Li, X.; Fang, Y.; Wang, J.; Wei, B.; Qi, K.; Hoh, H. Y.; Hao, Q.; Sun, T.; Wang, Z.; Yin, Z.; Zhang, Y.; Lu, J.; Bao, Q.; Su, C. High-Yield Electrochemical Production of Large-Sized and Thinly Layered NiPS3 Flakes for Overall Water Splitting. *Small* **2019**, *15*, No. 1902427.
- (46) Tong, Y.; Chen, P.; Chen, L.; Cui, X. Dual Vacancies Confined in Nickel Phosphosulfide Nanosheets Enabling Robust Overall Water Splitting. *ChemSusChem* **2021**, *14*, 2576–2584.
- (47) Luxa, J.; Cintl, S.; Spejchalová, L.; Lin, J. Y.; Sofer, Z. Potential Dependent Electrochemical Exfoliation of NiPS<sub>3</sub> and Implications for Hydrogen Evolution Reaction. *ACS Appl. Energy Mater.* **2020**, *3*, 11992–11999.
- (48) Thi, L. L. D.; Tuyen, P. N. K.; Vu, T. Y. Flower-like S-Doped-Ni2P Mesoporous Nanosheet-Derived Self-Standing Electrocatalytic Electrode for Boosting Hydrogen Evolution. *Nanotechnology* **2020**, *31*, No. 465401.
- (49) He, M.; Feng, C.; Liao, T.; Hu, S.; Wu, H.; Sun, Z. Low-Cost Ni<sub>2</sub>P/Ni<sub>0.96</sub>S Heterostructured Bifunctional Electrocatalyst toward Highly Efficient Overall Urea-Water Electrolysis. *ACS Appl. Mater. Interfaces* **2020**, *12*, 2225–2233.
- (50) Xiao, Z.; Huang, Y. C.; Dong, C. L.; Xie, C.; Liu, Z.; Du, S.; Chen, W.; Yan, D.; Tao, L.; Shu, Z.; Zhang, G.; Duan, H.; Wang, Y.; Zou, Y.; Chen, R.; Wang, S. Operando Identification of the Dynamic Behavior of Oxygen Vacancy-Rich Co<sub>3</sub>O<sub>4</sub>for Oxygen Evolution Reaction. *J. Am. Chem. Soc.* **2020**, *142*, 12087–12095.
- (51) Anantharaj, S.; Noda, S. Appropriate Use of Electrochemical Impedance Spectroscopy in Water Splitting Electrocatalysis. *Chem-ElectroChem* **2020**, *7*, 2297–2308.
- (52) Patil, S. J.; Chodankar, N. R.; Hwang, S.-K.; Rama Raju, G. S.; Huh, Y.-S.; Han, Y.-K. Fluorine Engineered Self-Supported Ultrathin 2D Nickel Hydroxide Nanosheets as Highly Robust and Stable Bifunctional Electrocatalysts for Oxygen Evolution and Urea Oxidation Reactions. *Small* **2022**, *18*, No. 2103326.
- (53) Li, J.; Liu, H. X.; Gou, W.; Zhang, M.; Xia, Z.; Zhang, S.; Chang, C. R.; Ma, Y.; Qu, Y. Ethylene-Glycol Ligand Environment Facilitates Highly Efficient Hydrogen Evolution of Pt/CoP through Proton Concentration and Hydrogen Spillover. *Energy Environ. Sci.* **2019**, *12*, 2298–2304.
- (54) Zhao, T.; Shen, X.; Wang, Y.; Hocking, R. K.; Li, Y.; Rong, C.; Dastafkan, K.; Su, Z.; Zhao, C. In Situ Reconstruction of V-Doped Ni<sub>2</sub>P Pre-Catalysts with Tunable Electronic Structures for Water Oxidation. *Adv. Funct. Mater.* **2021**, *31*, No. 2100614.
- (55) Morales, D. V.; Astudillo, C. N.; Anastasoaie, V.; Dautreppe, B.; Urbano, B. F.; Rivas, B. L.; Gondran, C.; Aldakov, D.; Chovelon, B.; André, D.; Putaux, J. L.; Lancelon-Pin, C.; Sirach, S.; Ungureanu, E. M.; Costentin, C.; Collomb, M. N.; Fortage, J. A Cobalt Oxide—Polypyrrole Nanocomposite as an Efficient and Stable Electrode

Material for Electrocatalytic Water Oxidation. Sustainable Energy Fuels **2021**, *5*, 4710-4723.

- (56) Hu, Z.; Wu, Z.; Han, C.; He, J.; Ni, Z.; Chen, W. Two-Dimensional Transition Metal Dichalcogenides: Interface and Defect Engineering. Chem. Soc. Rev. 2018, 47, 3100-3128.
- (57) Muthurasu, A.; Maruthapandian, V.; Kim, H. Y. Metal-Organic Framework Derived Co<sub>3</sub>O<sub>4</sub>/MoS<sub>2</sub> Heterostructure for Efficient Bifunctional Electrocatalysts for Oxygen Evolution Reaction and Hydrogen Evolution Reaction. Appl. Catal., B 2019, 248, 202-210.
- (58) Teng, Y.; Wang, X.-D.; Liao, J.-F.; Li, W.-G.; Chen, H.-Y.; Dong, Y.-J.; Kuang, D.-B. Atomically Thin Defect-Rich Fe-Mn-O Hybrid Nanosheets as High Efficient Electrocatalyst for Water Oxidation. Adv. Funct. Mater. 2018, 28, No. 1802463.
- (59) Liu, T.; Li, A.; Wang, C.; Zhou, W.; Liu, S.; Guo, L. Interfacial Electron Transfer of Ni<sub>2</sub>P-NiP<sub>2</sub> Polymorphs Inducing Enhanced Electrochemical Properties. Adv. Mater. 2018, 30, No. 1803590.

# Recommended by ACS

Reducible Co3+-O Sites of Co-Ni-P-Ox on CeO2 Nanorods **Boost Acidic Water Oxidation via Interfacial Charge Transfer-Promoted Surface Reconstruction** 

Jianyun Liu, Qing Li, et al.

MARCH 30, 2023 ACS CATALYSIS

READ

Ultrathin NiPt Single-Atom Alloy for Synergistically **Accelerating Alkaline Hydrogen Evolution** 

Liuxiang Huo, Zhigao Hu, et al.

NOVEMBER 23, 2022

ACS APPLIED ENERGY MATERIALS

READ

Ternary Ni-Co-Se Nanostructure for Electrocatalytic **Oxidative Value Addition of Biomass Platform Chemicals** 

Souradip Ganguly, Sirshendu Ghosh, et al.

MAY 10, 2023

ACS APPLIED ENERGY MATERIALS

READ

Heterostructured Palladium-Nickel Sulfide on Plasma-**Activated Nickel Foil for Robust Hydrogen Evolution** 

Xin Liu, Kostya Ostrikov, et al.

JUNE 03, 2022

ACS SUSTAINABLE CHEMISTRY & ENGINEERING

READ

Get More Suggestions >